A neutrophil timer coordinates immune defense and vascular protection

José M. Adrover [1], Carlos del Fresno [2], Georgiana Crainiciuc [1], Maria Isabel Cuartero [3], María Casanova-Acebes [1] †, Linnea A. Weiss [1] ‡, Hector Huerga Encabo [4], Carlos Silvestre-Roig [5], Jan Rossaint [6], Itziar Cossío [1], Ana V. Lechuga-Vieco [2], Jaime García-Prieto [2], Mónica Gómez-Parrizas [2], Juan A. Quintana [1], Ivan Ballesteros [1], Sandra Martin-Salamanca [1], Shu Zhen Chong [7], Maximilien Evrard [7], Karl Balabanian [8], Jorge López [9], Kiril Bidzhekov [5], Françoise Bachelerie [8], Francisco Abad-Santos [10], Cecilia Muñoz-Calleja [9], Alexander Zarbock [6], Oliver Soehnlein [5], Christian Weber [5,11], Lai Guan Ng [7], Cristina Lopez-Rodriguez [4], David Sancho [2], María A. Moro [3], Borja Ibáñez [2, 12] and Andrés Hidalgo [1, 5 *]

1 Area of Developmental and Cell Biology, Centro Nacional de Investigaciones Cardiovasculares Carlos III (CNIC), Madrid, Spain
2 Area of Myocardial pathophysiology, Centro Nacional de Investigaciones Cardiovasculares Carlos III (CNIC), Madrid, Spain
3 Unidad de Investigación Neurovascular, Department of Pharmacology, Faculty of Medicine, Universidad Complutense and Instituto de Investigación Hospital 12 de Octubre (i+12), Madrid, Spain
4 Immunology Unit, Department of Experimental and Health Sciences, Pompeu Fabra University, Barcelona
5 Institute for Cardiovascular Prevention (IPEK), Ludwig-Maximillians-Universität München and German Centre for Cardiovascular Research (DZHK), partner site Munich Heart Alliance, Munich, Germany
6 Department of Anesthesiology, Intensive Care, and Pain Medicine, University of Münster, Germany
7 Singapore Immunology Nework (SIgN), A*STAR, Biopolis, Singapore
8 Inserm Unité Mixte de Recherche (UMR) S996, Université Paris-Sud, Laboratory of Excellence in Research on Medication and Innovative Therapeutics, Clamart, France
9 Department of Immunology, Instituto de Investigación Sanitaria Princesa, Hospital Universitario de La Princesa, Madrid, Spain
10 Department of Clinical Pharmacology, Instituto Teófilo Hernando, Hospital Universitario de la Princesa, Instituto de Investigación Sanitaria Princesa, Madrid, Spain
11 Dept. of Biochemistry, Cardiovascular Research Institute Maastricht (CARIM), Maastricht University, Maastricht, the Netherlands.
12 CIBER de enfermedades Cardiovasculares (CIBERCV), Madrid, Spain; and Department of Cardiology, Instituto de Investigación Sanitaria (IIS)-Fundación Jiménez Díaz, Madrid, Spain.

† Current affiliation: Tisch Cancer Institute, Mount Sinai School of Medicine, NY

‡ Current affiliation: Centro Nacional de Biotecnología, Madrid, Spain

*Correspondence and Lead Contact: Andrés Hidalgo (ahidalgo@cnic.es)

Area of Cell & Developmental Biology, Fundación CNIC, Calle Melchor Fernández Almagro 3, 28029 Madrid, Spain. Phone: +34 91 4531200 (Ext. 1504). Fax: +34 91 4531245

Summary

Neutrophils eliminate pathogens efficiently, but can inflict severe damage to the host if they over-activate within blood vessels. It is unclear how immunity solves the dilemma of mounting an efficient anti-microbial defense while preserving vascular health. Here, we identify a neutrophil-intrinsic program that enables both. The gene *Bmal1* regulated expression of the chemokine CXCL2 to induce CXCR2-dependent diurnal changes in the transcriptional and migratory properties of circulating neutrophils. These diurnal alterations, referred to as neutrophil aging, were antagonized by CXCR4 and regulated the outer topology of neutrophils to favor homeostatic egress from blood vessels at night, resulting in boosted anti-microbial activity in tissues. Mice engineered for constitutive neutrophil aging became resistant to infection, but the persistence of intravascular aged neutrophils predisposed to thrombo-inflammation and death. Thus, diurnal compartmentalization of neutrophils, driven by an internal timer, coordinates immune defense and vascular protection.

Introduction

The capacity of neutrophils to kill pathogens but to also inflict severe damage to tissues suggests the existence of a protective mechanism that balances these opposing functions. Both anti-microbial immunity and vascular inflammation are known to follow circadian patterns (Man et al., 2016; Muller et al., 1989; Scheiermann et al., 2013), suggesting that such mechanism may be temporally regulated. The nature of this mechanism, however, remains enigmatic. While studying neutrophils in the steady-state we previously identified a natural phenotypic shift of circulating neutrophils that followed a strict diurnal regime (Casanova-Acebes et al., 2013). Neutrophils released from the bone marrow display high levels of CD62L that are progressively and spontaneously reduced during the day, while the levels of CXCR4 increase prior their natural egress from blood, or clearance (Casanova-Acebes et al., 2013). In a small cohort of healthy volunteers, we confirmed that similar diurnal phenotypic changes occur in circulating neutrophils in humans, indicating conservation of this phenomenon across species (Figure S1A). This process, referred to as *neutrophil aging*, has been proposed to be regulated by the gut microbiota and to favor a pro-inflammatory phenotype that predisposes to vascular inflammation (Zhang et al., 2015). Contrasting with this model of extrinsically-driven neutrophil aging, various lines of evidence have shown that intrinsic programs controlled by the molecular clock also regulate the properties of immune cells, including macrophages, monocytes or T cells (Druzd et al., 2017; Nguyen et al., 2013; Silver et al., 2012). Because the mechanisms regulating aging and the consequences of this process in physiology remain uncertain, we set out to explore whether neutrophils are endowed with an intrinsic program that controls diurnal aging, tunes their anti-microbial functions, and limits vascular inflammation.

By comparing the transcriptome of circulating neutrophils at different diurnal times we found regulation of clock-related genes and the CXCR2 signaling pathway. We show that Bmal1 (brain and muscle aryl hydrocarbon receptor nuclear translocator (ARNT)-like 1; encoded by *Arntl*) regulated expression of CXCL2, a CXCR2 ligand that controlled neutrophil aging in a cell-

autonomous manner. Deletion of Bmal1 or *Cxcr2* from neutrophils prevented phenotypic aging, whereas deletion of *Cxcr4*, a negative regulator of CXCR2 signaling (Martin et al., 2003), resulted in unrestrained aging. Analyses of mice lacking these genes in neutrophils, or wild-type mice at different diurnal times, demonstrated that aging disrupts cytoskeletal integrity to specifically prevent rolling and accumulation in inflamed areas, without affecting the homeostatic migration of aged neutrophils into naïve tissues at night. We show that this temporal regulation of neutrophil trafficking regulated diurnal responses to infections, while at the same time clearing neutrophils out of the bloodstream thereby protecting the vasculature from inflammatory injury. These findings uncover a mechanism that protects host tissues even in the presence of a fully competent anti-microbial immunity, is intrinsic to neutrophils, and that may explain the circadian susceptibility of mammals to cardiovascular disease.

Results

A neutrophil-intrinsic timer drives diurnal aging

In healthy mice, the number of aged neutrophils in blood follows diurnal patterns with a peak at around zeitgeber time 5 (ZT5; i.e. 5 hours after the onset of light), while non-aged neutrophils (referred to as “fresh”) predominate at ZT13 (Casanova-Acebes et al., 2013). These diurnal patterns persisted in constant darkness and could be entrained by a light-shift (Figure S1B-C), indicating that neutrophil aging is a *bona fide* circadian process. To identify genetic programs that were temporally regulated in neutrophils we first compared the transcriptomes of circulating neutrophils purified from wild-type mice at these two times. We identified changes in over 1300 genes related to pathways of inflammation, migration and apoptosis (Figure 1A-B and Table S1), which suggested natural modulation of these processes during the day. We validated expression for a group of selected genes by quantitative PCR (Figure S1D). Given the diurnal

pattern of aging, we also inspected genes of the molecular clock as they are known to regulate diurnal rhythms of the immune system (Man et al., 2016; Scheiermann et al., 2013). Expression of several clock-related genes, including *Arntl* (encoding Bmal1) or *Clock* increased at ZT5, while others like *Per2* were decreased at this time (Figure 1B and S1D-E). Interestingly, transcriptional analyses at multiple times of day revealed circadian oscillations for all these genes in circulating neutrophils (Figure 1C). Our RNA sequencing analyses further demonstrated reduced expression of *Sell* (encoding CD62L) at ZT5, but no changes for *Cxcr4* (Figure 1B). We also noticed reduced expression of *Cxcr2* at ZT5 (Figure 1B), whose expression, like the clock genes, displayed a diurnal pattern (Figure 1D). This finding was intriguing because CXCR2 agonists induced phenotypic changes in neutrophils that resembled those seen during natural aging, namely reductions in CXCR2 and CD62L surface levels (Figure 1E and Figure S1F).

Guided by the temporal expression patterns of this set of genes and their reported functions in various immune settings (Eash et al., 2010; Mei et al., 2012; Nguyen et al., 2013), we predicted that Bmal1 and CXCR2 might be required for diurnal neutrophil aging. Although CXCR4 did not present transcriptional oscillations (Figure 1D), its surface levels on neutrophils changed diurnally (Figure 1E and (Casanova-Acebes et al., 2013)) and CXCR4 is known to antagonize CXCR2 signaling (Martin et al., 2003), suggesting that this receptor might also contribute to aging. Because diurnal aging occurs in the circulation, we examined whether the main physiological agonists for CXCR2 and CXCR4 were present in blood at steady-state. Ligands for both receptors were detectable in the plasma of wild-type mice, with oscillating amounts of CXCL12, and low but detectable levels of CXCL2 (Figure 1F).

To formally test the possibility that these genes regulated neutrophil aging, we generated mice with neutrophil-specific deficiency in *Arntl*, *Cxcr2* or *Cxcr4* (herein referred to as Bmal1$^{\Delta N}$, CXCR2$^{\Delta N}$ and CXCR4$^{\Delta N}$) using the MRP8^{CRE} driver line, which resulted in robust depletion of the

receptors form the surface of neutrophils (Figure S2A-B). Western blot analysis of Bmal1 protein confirmed efficient depletion in Bmal1$^{\Delta N}$ neutrophils, and revealed reductions of this protein at ZT13 in wild-type neutrophils but unchanged levels in CXCR2$^{\Delta N}$ and CXCR4$^{\Delta N}$ neutrophils (Figure S2C). We then assessed surface levels of CD62L, a marker whose levels decline during aging ((Casanova-Acebes et al., 2013; Uhl et al., 2016; Zhang et al., 2015) and Figure 1E). To ensure that potential alterations were cell-intrinsic, we generated bone marrow transplant chimeras of wild-type and each of the mutant donors. We found elevated levels of CD62L in circulating neutrophils from Bmal1$^{\Delta N}$ and CXCR2$^{\Delta N}$ donors, suggesting disrupted aging in these mutants (Figure 2A). In contrast, CXCR4$^{\Delta N}$ neutrophils were low for CD62L, which suggested constitutive aging (Figure 2A). If these alterations were caused by disruption of diurnal aging, we predicted that the levels of CD62L would not change over time. Indeed, *in vivo* metabolic pulse and chase of neutrophils with BrdU demonstrated that the temporal changes in CD62L levels seen in wild-type neutrophils were lost in Bmal1$^{\Delta N}$ and CXCR4$^{\Delta N}$ mutants (Figure 2B). To further confirm that these genes regulated the natural dynamics of aging, we measured the levels of CD62L through full diurnal cycles in all mutant mice. While CD62L levels exhibited diurnal oscillations in wild-type neutrophils, all three mutants presented disrupted patterns, with Bmal1$^{\Delta N}$ mutants showing a complete loss of rhythmicity (Figure 2C). Accordingly, the levels of CXCR4 in Bmal1$^{\Delta N}$ neutrophils also lost diurnal oscillations (not shown).

To dissect the antagonistic role of CXCR4 in aging, we pre-treated wild-type neutrophils with CXCL12, the main ligand for CXCR4, before exposing them to a CXCR2 agonist. Given the constitutively aged status of CXCR4-deficient neutrophils, we hypothesized that stimulation of CXCR4 would prevent CXCR2-dependent responses. Indeed, CXCL12 blunted both the reductions in CD62L and chemotaxis elicited through CXCR2 (Figure S2D). In addition, neutrophils expressing CXCR4^{WHIM}, a hyper-signaling variant of CXCR4 (Balabanian et al., 2012), displayed constitutive elevations in CD62L levels (Figure S2E), a finding consistent with

the notion that CXCR4 signaling prevents neutrophil aging. Combined, these data indicated that Bmal1 and CXCR2 promote diurnal aging, and that CXCR4 prevents it.

Aging-driven transcriptional programs

Having identified Bmal1, CXCR2 and CXCR4 as intrinsic regulators of diurnal aging, we used the neutrophil-specific mutant mice as models to examine how programmed diurnal aging impacted neutrophil physiology. We first performed transcriptomic analyses of blood neutrophils extracted from Bmal1$^{\Delta N}$, CXCR2$^{\Delta N}$ and CXCR4$^{\Delta N}$ mice at ZT5, and compared them with the profiles of wild-type neutrophils at ZT5 and ZT13. Principal component analyses of the five groups revealed that neutrophils that displayed a CD62L^{HI} fresh phenotype clustered together (including wild-type at ZT13, Bmal1$^{\Delta N}$ and CXCR2$^{\Delta N}$), whereas those that shared an aged phenotype (wild-type at ZT5 and CXCR4$^{\Delta N}$) separated from the “fresh” cluster (Figure 2D), with many genes differentially regulated among the fresh and aged groups (Figure S2F). Consistent with a role in diurnal aging, when we contrasted the transcriptomes of wild-type and mutant mice at both ZT5 and ZT13 we found that the diurnal changes in gene expression of wild-type neutrophils were absent or blunted in Bmal1$^{\Delta N}$ and CXCR4$^{\Delta N}$ neutrophils (Figure S2G). These findings aligned with the phenotypic data (Figure 2A and 2C) and, importantly, defined diurnal aging as a global transcriptional program of circulating neutrophils that occurs naturally during the day, and that could be recapitulated in the mutant mice.

We next focused our attention on genetic programs that consistently changed when independently interrogating the effect of time (ZT5 vs. ZT13) and genotype (Bmal1$^{\Delta N}$ vs. CXCR4$^{\Delta N}$). We noticed prominent regulation of the IL-8 signaling pathway (a ligand for human CXCR2; Figure S2H), which was in line with our previous results and further suggested engagement of CXCR2 during aging. Interestingly, analyses of our sequencing data revealed

that among aging-related genes only expression of *Cxcl2*, a CXCR2 ligand expressed by neutrophils (Li et al., 2016), was reduced in Bmal1$^{\Delta N}$ relative to wild-type neutrophils (Figure 2E), suggesting that this chemokine could provide a link between Bmal1 and CXCR2 during aging. Indeed, chromatin immunoprecipitation (ChIP) assays with wild-type neutrophils revealed that Bmal1 bound predicted E-box elements in the promoter regions not only of known target clock genes (*Per2* and *Nr1d1*), but also of the *Cxcl2* gene (Figure 2F). More importantly, analysis of bone marrow chimeras from wild-type and *Cxcl2*$^{-/-}$ donors confirmed that this chemokine was required for neutrophil aging in a cell-autonomous manner (Figure 2G). Consistent with this finding, *in vivo* blockade of CXCL2, but not CXCL1 (another ligand for CXCR2), blunted the aging phenotype of wild-type neutrophils without affecting CXCR2$^{\Delta N}$ mutants (Figure S2I). These findings explained the defective aging seen in Bmal1$^{\Delta N}$ neutrophils (Figure 2A), and revealed that Bmal1-driven production of CXCL2 controlled neutrophil aging through autocrine CXCR2 signaling.

To independently assess the cell-intrinsic nature of aging, we tracked the kinetics of fresh neutrophils transferred into recipient mice at ZT5 (i.e., at the time of maximal aging). While host mice became enriched in fresh neutrophils over time, the transferred neutrophils became progressively aged (Figure S2J), further supporting that neutrophil aging is intrinsically driven.

Taken together, these findings supported a model whereby diurnal neutrophil aging is driven by Bmal1 through regulation of *Cxcl2* expression. This chemokine in turn triggers autocrine CXCR2 signaling to drive changes associated with aging, whereas CXCR4 antagonizes these signals to prevent aging (Figure 2H). Importantly, because the CXCR4 ligand CXCL12 is produced by multiple cell types but not by neutrophils (Figure 2E), we conclude that both cell-intrinsic and –extrinsic factors contribute to neutrophil aging.

Aging-regulated migration of neutrophils

The transcriptomic analyses additionally identified pathways that changed significantly (-log (p-value)>1.3), including cytokine signaling, activation of nuclear receptors, toll-like receptor signaling, leukocyte extravasation or actin cytoskeleton signaling (Figure 1A and Figure S2H). Because many of these pathways ultimately regulate the migration of neutrophils into tissues to exert immune functions, we investigated the *in vivo* trafficking patterns associated with neutrophil aging.

We considered two migratory modalities that are relevant in neutrophil physiology: migration into healthy tissues (or clearance, a process that follows diurnal cycles (Casanova-Acebes et al., 2018; Scheiermann et al., 2012)), and migration into inflamed tissues. We took advantage of our neutrophil-specific mouse models to exclude cell-extrinsic factors influenced by time, such as diurnal changes in adhesion molecules reported on endothelial cells (Scheiermann et al., 2012). In addition, because CXCR2 plays prominent roles in multiple homeostatic and inflammatory scenarios that may not be related to aging, we restricted our subsequent analyses to Bmal1 and CXCR4 mutants as models for fresh and aged neutrophils, respectively.

We first generated parabiotic pairs of wild-type and mutant mice to compare the migration efficiency of fresh (Bmal1$^{\Delta N}$) and aged (CXCR4$^{\Delta N}$) neutrophils relative to wild-type neutrophils in the same physiological context (Figure 3A). We found that homeostatic clearance of Bmal1$^{\Delta N}$ neutrophils into multiple tissues of wild-type partners was strongly impaired, whereas it was unaffected for CXCR4$^{\Delta N}$ neutrophils (Figure 3B), indicating that neutrophil aging was required for clearance into tissues.

We next examined the migration of the aging mutant neutrophils into inflamed tissues using zymosan-induced peritonitis in the parabiotic pairs. Surprisingly, we found the opposite response: enhanced migration of Bmal1$^{\Delta N}$ fresh neutrophils and reduced infiltration by CXCR4$^{\Delta N}$ aged neutrophils (Figure 3C). Using an independent model of constitutive aging (mice lacking

endothelial selectins, or PEdKO mice; (Casanova-Acebes et al., 2013)) we confirmed that aged neutrophils displayed intact clearance at steady-state (Figure S3A), but impaired migration to inflamed tissues (Figure 3B). In contrast, impaired aging of neutrophils expressing the hyper-signaling CXCR4^{WHIM} mutation resulted in enhanced migration to inflamed tissues (Fig.S2E). Whole-mount imaging of inflamed cremasteric muscles from transplantation chimeras further confirmed the differential capacity of fresh and aged neutrophils to infiltrate inflamed tissues relative to wild-type cells after correction for relative numbers in blood (Figure 3D-E), and this became even more prominent when constitutively aged and fresh neutrophils expressing different fluorescent proteins were simultaneously compared within the same mouse (Figure 3F). Importantly, these findings aligned with enhanced inflammatory recruitment of wild-type neutrophils when they were phenotypically fresh (ZT13), and this diurnal preference was lost in Bmal1$^{\Delta N}$ and CXCR4$^{\Delta N}$ mutant mice (Figure S3B). These data revealed that aging profoundly influences the migratory capacity of neutrophils by causing a diurnal switch of migratory patterns from inflammatory (fresh neutrophils at ZT13 and Bmal1$^{\Delta N}$) to homeostatic (aged neutrophils at ZT5 and CXCR4$^{\Delta N}$).

Surface topology and rolling efficiency are regulated during diurnal aging

To search for the mechanisms underlying the distinct migratory patterns of fresh and aged neutrophils, we examined the different steps of the recruitment cascade (rolling, adhesion and extravasation) in the cremasteric microcirculation by intravital microscopy (Figure 4A). We found elevated rolling, adhesion and extravasation efficiencies of Bmal1$^{\Delta N}$ neutrophils, and significant reductions for CXCR4$^{\Delta N}$ neutrophils (Figure 4B). The defects in the recruitment cascade of CXCR4$^{\Delta N}$ aged neutrophils could be independently reproduced in PEdKO-derived aged neutrophils (Figure S4A and Movie S1). In contrast to rolling, however, the crawling dynamics of

neutrophils on the vessel wall and within tissues (Figure S4B-C), as well as the migration to various chemoattractants (Figure S4D), were comparable among all groups. To determine whether the alterations in rolling seen in mutant cells also occurred in wild-type neutrophils, and to avoid confounding diurnal changes in parenchymal cells, we imaged auto-perfused flow chambers coated with P-selectin alone or together with ICAM-1 and CXCL1, and connected to the circulation of wild-type mice at ZT5 and ZT13 (Figure S4E). In agreement with the data in the mutant models, we found elevated rolling efficiencies and subsequent adhesion for neutrophils at ZT13 relative to ZT5 (Figure S4F), indicating that diurnal changes in rolling and adhesion were cell-intrinsic. Combined, these data suggested that diurnal aging impaired inflammatory recruitment by specifically targeting rolling, a rate-limiting step during leukocyte recruitment (Ley et al., 2007).

Because rolling is largely mediated by endothelial selectins, the data implied that aging targeted selectin ligands on neutrophils. Unexpectedly, binding analyses using soluble P- and E-selectin antibody chimeras revealed only modest changes in selectin binding activity regardless of time of day or genetic background (Figure S4G), suggesting that biosynthesis of selectin ligands was unlikely to cause the loss of rolling during aging. Effective engagement of selectins under flow, however, additionally demands correct topology at the neutrophil's surface to optimize ligand presentation at the tip of microvilli, a type of membrane protrusion that relies on a network of cortical actin (Finger et al., 1996; Simon et al., 2007; von Andrian et al., 1995). Analyses of actin distribution by immunofluorescence staining and surface topology by scanning electron microscopy revealed that aged neutrophils displayed dramatic reductions in cortical β-actin, which coincided with reduced number of microvilli both in wild-type mice at ZT5 (Figure 4C-D), and in genetically-induced aged mice ($CXCR4^{\Delta N}$; Figure S4H-I). These data revealed that disruption of the neutrophil's cortical architecture during aging impairs migration to inflamed tissues.

Homeostatic migration does not require rolling

These observations, however, failed to explain why poorly-rolling aged neutrophils maintained an intact capacity to enter non-inflamed tissues under homeostasis (Figure 3B). To address this question, we analyzed homeostatic and inflammatory recruitment in control mice, and in mice in which vessels do not support rolling due to the lack of endothelial selections (PEdKO mice; (Frenette et al., 1996)). While adhesion to inflamed vessels required selectin-mediated rolling as expected, we were surprised to find that spontaneous adhesion during homeostatic recruitment to the skin occurred even in the absence of rolling (Figure 4E). Video analyses of the dermal microvasculature at times of clearance (ZT9) confirmed that neutrophils arrested suddenly, without the need of a preceding rolling step (Figure 4F and Movie S2). Thus, neutrophil aging maintains homeostatic clearance but prevents inflammatory recruitment by disabling selectin-mediated rolling (Figure 4G).

To determine how the differential migratory properties of fresh and aged neutrophils affected tissue injury, we induced ischemic inflammation of the brain by occlusion of the middle cerebral artery. Because the brain is devoid of neutrophils at steady-state (Figure S4J), this model allows measuring the contribution of infiltrating neutrophils to tissue damage (Cuartero et al., 2013; Sreeramkumar et al., 2014). In line with our prediction, brain injury was only exacerbated in Bmal1$^{\Delta N}$ mice enriched in fresh neutrophils (Figure S4K), suggesting that preferential migration of fresh neutrophils during inflammation contributes to tissue injury.

Diurnal aging boosts anti-microbial defense

The observations so far raised the possibility that regulation of neutrophil migration during the day might be a primary role of diurnal aging; it could drive compartmentalization of aged neutrophils into tissues at night in anticipation of pathogens potentially breaking into tissues,

while at the same time reducing their numbers within vessels to minimize injury when the chance of immune activation is higher.

To address this possibility, we analyzed the diurnal dynamics of aged neutrophils in the circulation of wild-type and mutant mice throughout the day. The analyses revealed striking differences: in wild-type mice aged neutrophils peaked at ZT5 and disappeared at ZT13, while in Bmal1$^{\Delta N}$ mice they displayed non-oscillating low levels, and CXCR4$^{\Delta N}$ animals presented constitutively high numbers of aged neutrophils in blood (Figure 5A). Interestingly, the absolute number of neutrophils maintained normal oscillations in the blood of Bmal1$^{\Delta N}$ mutants (Figure S5A), indicating that neutrophil numbers and aging are regulated through different mechanisms. We therefore used these mouse models to determine how the diurnal migratory fluxes driven by neutrophil aging regulated immune defense and vascular health.

We first infected mice with *Candida albicans*, using a protocol that allows systemic spread, targets the kidneys, and is controlled by neutrophils (Lionakis et al., 2011). Wild-type mice displayed diurnal patterns of response to infection, with increased resistance at ZT13 as defined by reduced weight loss, fungal load in kidneys and improved survival, (Figure 5B and Figure S5B-C). Importantly, the initial time of infection was critical for the long-term immune response because the effect could be seen several days after infection. Resistance to *Candida* at ZT13 coincided with more neutrophils in naïve kidneys and fewer in blood (Figure S5D-E), suggesting that their presence in tissues at the time of infection conferred protection. Remarkably, we found that the diurnal variation in susceptibility to *Candida* infection was abolished in Bmal1$^{\Delta N}$ mice (Figure 5C), indicating that neutrophil aging was needed to anticipate the infection. These observations predicted that mice with constitutively aged neutrophils clearing into tissues might perform better against infection. In agreement with this possibility, CXCR4$^{\Delta N}$ mice had more neutrophils in naïve kidneys and manifested remarkable resistance to infection and reduced

fungal spread (Figure 5D-F). However, because we noted that CXCR4$^{\Delta N}$ mice displayed neutrophilia (Figure S5A), this observation could be alternatively explained by elevated numbers rather than the aging status of neutrophils. To discriminate between these possibilities, we treated wild-type mice with a single injection of the CXCR4 antagonist AMD3100, a treatment that causes acute neutrophilia (Devi et al., 2013) but did not induce aging (Figure S5F-G). Despite neutrophil counts that were even higher than those in CXCR4$^{\Delta N}$ mice, AMD3100-treated mice were as susceptible to *Candida* infection as untreated wild-type mice (Figure 5G), indicating that the aging status rather than the number of neutrophils conferred protection against *Candida*. In addition, the capacity of fresh (ZT13 or Bmal1$^{\Delta N}$) and aged (ZT5 and CXCR4$^{\Delta N}$) neutrophils to phagocytose *Candida* conidia, to produce reactive oxygen species (Figure S5H-J), to secrete cytokines (Figure S5K) as well as their metabolic status (mitochondrial respiration and glycolysis; not shown) were similar to wild-type cells, which supported the contention that neutrophil migration, rather than other cellular processes, was the relevant process regulated by aging. We obtained evidence of similar diurnal variations in the response to bacterial sepsis, which was also lost in Bmal1$^{\Delta N}$ mice (Figure S5L), further revealing a general influence of neutrophil aging in responses to infection. Thus, aging-driven clearance of neutrophils into tissues orchestrates anti-microbial defense.

Constitutive neutrophil aging predisposes to vascular inflammation

To define whether diurnal neutrophil aging additionally conferred protection to vessels, we used a model of acute myocardial infarction (AMI) induced by ischemia-reperfusion of the left anterior descending coronary artery. In this model, early inflammation originates intravascularly without prior neutrophil extravasation (Vinten-Johansen, 2004). Similar to infections, the extent of cardiac damage in wild-type mice displayed diurnal variations, with larger infarct size when surgery was performed at ZT5, after correction for the area at risk (Figure 6A-B and Figure

S6A). Accordingly, infarct sizes after only one hour of reperfusion were remarkably larger in CXCR4$^{\Delta N}$ mice and smaller in Bmal1$^{\Delta N}$ mice (Figure 6C), and this correlated with all CXCR4$^{\Delta N}$ mice succumbing (11 of 11) by 24 hours post-surgery (Figure 6D). This dramatic response agreed with the reported involvement of aged neutrophils in other forms of vascular inflammation (Zhang et al., 2015), and again was not caused by increased numbers of circulating neutrophils in CXCR4$^{\Delta N}$ mice because treatment of wild-type mice with AMD3100 did not aggravate myocardial injury (Figure 6E). These data indicated that the excessive presence of aged neutrophils in the circulation was detrimental for the myocardial tissue after vascular ischemia and reperfusion, and that their diurnal clearance was protective.

Although massive cardiomyocyte death driven by intravascular aged neutrophils seemed to account for the extreme susceptibility of CXCR4$^{\Delta N}$ mice during AMI, we examined other potential mechanisms by which aged neutrophils might exacerbate vascular injury. Using a model of ischemia-reperfusion in the cremasteric muscle that allows high resolution live imaging of affected vessels, we found disseminated thrombi in microvessels of CXCR4$^{\Delta N}$ mice (Figure S6C and Movie S3). Depletion of neutrophils in CXCR4$^{\Delta N}$ mice prevented thrombi formation and improved survival after infarction (Figure S6B-C), indicating that both responses were mediated by neutrophils. Although neutrophil extracellular traps (NET) can promote thrombosis (Fuchs et al., 2010), they were not responsible for the response of CXCR4$^{\Delta N}$ mice because two different NET inhibitors failed to prevent thrombi formation in reperfused venules (Figure S6D). In addition, endothelial proliferation and apoptosis as well as vascular permeability were not affected at baseline across multiple tissues, including hearts, of Bmal1$^{\Delta N}$ and CXCR4$^{\Delta N}$ mice (Figure S6E-G), indicating that aging did not directly compromise basal vascular health prior the ischemic insult.

Overall, these observations are consistent with the known circadian susceptibility of humans to AMI at specific times of day (Muller et al., 1989), particularly in the early morning when aged

neutrophils appear in the human circulation (Figure S1A). In addition, because aged neutrophils predominate at ZT5 and CXCR4$^{\Delta N}$ mice display constant high numbers of aged neutrophils in blood (Figure 5A), the data suggests that diurnal compartmentalization of aged neutrophils into tissues and out of the circulation confers vascular protection (Figure 6F and Movie S4).

Discussion

Mammalian immunity is not constant in number or quality throughout the day, as it adapts to varying diurnal challenges from the environment, including the chance of exposure to infectious pathogens (Man et al., 2016). Likewise, it has been long appreciated that damage to the cardiovascular system, in both humans and model organisms, follows circadian patterns (Muller et al., 1989; Scheiermann et al., 2013). Because neutrophils are major mediators of anti-microbial defense and vascular inflammation, we predicted that the diurnal variations in both processes could be mechanistically explained by the existence of a neutrophil-intrinsic temporal program (referred here as "timer") that regulated their activity through the day. In this study, we identify and characterize this program and show that it underlies the circadian susceptibility of mice to infection and vascular inflammation. Although we cannot formally exclude other mechanisms that control the diurnal properties of neutrophils, we have failed to find defects in neutrophil aging in mice with defective ROS production (data not shown) or depleted of microbiota (Figure S6H-K), both of which had been previously associated with neutrophil senescence or aging, respectively (Harbort et al., 2015; Zhang et al., 2015).

An internal timer that coordinates defense and inflammation

We have found that the diurnal program of neutrophils is coordinated by the circadian-associated protein Bmal1 in coordination with two chemokine receptors, CXCR2 which drives aging, and CXCR4 which antagonizes it. Multiple functional assays allowed us to confirm that time-of-day differences in wild-type cells could be faithfully recapitulated by the respective

mutants: Bmal1$^{\Delta N}$ cells resembled night (fresh) neutrophils whereas CXCR4$^{\Delta N}$ mutants behave similar to daytime (aged) neutrophils. Before release into the bloodstream, maturing neutrophils are retained within the marrow in an environment with high CXCR4/CXCL12 signaling (Eash et al., 2010; Eash et al., 2009), which raises the intriguing possibility that this diurnal timer may be inhibited until neutrophils are released into blood. Once in blood, functional analyses of mice in which we disabled each component of this timer revealed that preferential invasion of inflamed or naïve tissues is compartmentalized in time. Under steady-state conditions, neutrophils released from the marrow gradually lose their ability to enter inflammatory sites and prepare for clearance into tissues. This migratory switch is intrinsically regulated, but it likely coordinates with extrinsic programs because disruption of rhythms in vascular cells can also affect the diurnal entry of leukocytes in tissues (Scheiermann et al., 2012) and because CXCL12, which is not produced by neutrophils, negatively regulates diurnal aging through CXCR4.

We find that one potential benefit of diurnal infiltration into naïve tissues is to optimize immune defense, as demonstrated by the loss of diurnal oscillations in the response against fungal or bacterial infections when Bmal1 was deleted from neutrophils. Removal of CXCR4, the negative regulator of the neutrophil timer, instead caused unrestrained aging and enhanced anti-microbial responses, while at the same time precipitating severe thrombo-inflammatory reactions following ischemia-reperfusion. In contrast, Bmal1$^{\Delta N}$ mutants displayed attenuated damage during myocardial infarction, altogether indicating that an intact neutrophil clock is important to balance anti-microbial defense and cardiovascular inflammation.

An additional, unexpected finding was that the aging status, rather than the number of circulating neutrophils, was the parameter that best predicted immune and inflammatory responses, at least in the models used in this study. This finding agrees with reports suggesting that aged neutrophils favor vascular inflammation (Zhang et al., 2015), and with the growing appreciation that heterogeneity among neutrophils is functionally relevant (Silvestre-Roig et al.,

2016). In particular, we report here a type of heterogeneity that, unlike that found in autoimmunity or cancer (Nicolas-Avila et al., 2017), associates with time-of-day in the steady-state. We do not know whether the aging phenotypes reported here relate with low/high density neutrophils or other subsets found in specific scenarios, yet defining this relationship may be key to predict possible time-dependent contributions of neutrophils during cancer or chronic inflammation.

The diurnal timer as a regulator of migration

Among the various transcriptional pathways activated during aging we identified those related to leukocyte extravasation and actin cytoskeleton signaling, an observation that allowed us to identify disruption of cortical actin polymerization as a key molecular event linking diurnal aging with alterations in the migratory properties of neutrophils. While the mechanisms underlying these cytoskeletal changes remain to be elucidated, this observation is consistent with early studies showing disrupted actin polymerization on human $CD62L^{LO}$ neutrophils (Tanji-Matsuba et al., 1998). Diurnal loss of microvilli was particularly relevant because these structures allow presentation of glycoconjugate ligands to endothelial selectins under flow (von Andrian et al., 1995), thus explaining the dramatic loss of rolling and migration of aged neutrophils to inflamed areas. At the same time, loss of microvilli might conceivably enhance the exposure of β2 integrins present on the cell body (Erlandsen et al., 1993) and favor rolling-independent arrest as seen in the naïve dermal microvasculature. We find it intriguing that a similar behavior of constitutive adhesion in non-inflamed vessels is displayed by patrolling monocytes (Auffray et al., 2007), suggesting that this mechanism could be a common property of myeloid leukocytes endowed with homeostatic surveillance roles. These observations should incite revision of the classical recruitment cascade, which for myeloid leukocytes has been almost exclusively studied in the context of inflammation (Ley et al., 2007), but may differ in significant ways during homeostasis.

A diurnal clock or a timer?

Overall, our findings are consistent with a model in which the oscillatory nature of the aging program enables alert states of neutrophils that are useful to anticipate infections, but must be shut down when the risk of infection is low to prevent damage to the vasculature. Interestingly, Bmal1-driven aging of neutrophils may not necessarily adjust to behavioral rhythms since we find that neutrophil aging peaks in the morning in both humans and mice, which are species with opposed activity periods. We therefore propose that a major purpose of aging could be to ensure temporal separation of neutrophil-mediated responses within vessels from those in tissues, thereby optimizing defense without compromising vascular health.

The diurnal aging pattern of neutrophils aligns with studies showing temporally gated responses for other leukocyte subsets, including monocytes, macrophages or Th17 cells (Nguyen et al., 2013; Silver et al., 2012; Yu et al., 2013), which may be useful to temporally concentrate immune response against specific pathogens in different tissues (Tognini et al., 2017). Different from these other types of leukocytes, however, the existence of a circadian program in neutrophils was not intuitive because their lifetime in the circulation is generally accepted to be less than one day (Summers et al., 2010), which implies that there cannot be true circadian oscillations of gene expression within a given neutrophil. Further, at present we do not know whether aging is regulated by the transcriptional properties of Bmal1 or by the core circadian clock. For these reasons, we envision this system to function like a cellular timer (rather than a true circadian clock) that resets with every new wave of neutrophils released from the bone marrow. In other words, for short-lived cells such as neutrophils, the clock appears to regulate oscillations on a population scale, by acting as a timer at the cellular level.

Therapeutic manipulation of the neutrophil timer

Given the high prevalence of infections and cardiovascular disease, a final question is whether the identification of a diurnal program in neutrophils could offer therapeutic alternatives for these

life-threatening complications. In principle, targeting the pro-aging receptor (CXCR2) or the anti-aging receptor (CXCR4) with specific agonists might allow pharmacological and transient manipulation of the timer. This type of “chrono-programming” of neutrophils could allow the generation of phenotypes that promote defense or protect the vasculature, as needed. We expect that manipulation of the timer will not have detrimental consequences because animals with impaired or enhanced neutrophil aging do not present gross anomalies or spontaneous susceptibility to disease at baseline, at least under specific-pathogen free conditions (data not shown). Thus, for humans at risk of cardiovascular events it might be advisable to block aging, whereas immune-compromised patients susceptible to infections might benefit from drugs that promote aging. We are currently exploring strategies that exploit the unique temporal properties of neutrophils.

Author contribution: J.M.A., C.dF., M.I.C., M.C-A, L.A.W., H.H.E., C.S-R., J.R., J.A.Q., G.C., J.G-P., M.G.P., D.G.M., S.M-S., M.E., J.L. performed experiments; C.W., K.B. and F.B. contributed essential reagents; A.Z., O.S., C.L-R., M.A.M., B.I., D.S., L.N., J.M.A. and A.H. designed and supervised experiments; F.A. and C.M. coordinated the study on humans; A.H. designed and supervised the study. A.H. and J.M.A. wrote the manuscript, which was edited by all authors.

Acknowledgments:

We thank all members of the Hidalgo Lab for discussion and insightful comments; J. M. Ligos, R. Nieto and M. Vitón for help with sorting and cytometric analyses; I. Ortega and E. Santos for animal husbandry; D. Rico, M. J. Gómez, C. Torroja and F. Sanchez-Cabo for insightful comments and help with transcriptomic analyses; V. Labrador, E. Arza, A. M. Santos and the Microscopy Unit of the CNIC for help with microscopy; S. Aznar-Benitah, U. Albrecht, Q-J. Meng, B. Staels and H. Duez for the generous gift of mice; J.A. Enriquez and J. Ávila for scientific insights and J. M. García and A. Diez de la Cortina for art. The data is presented in the main manuscript and in the supplementary materials. RNA-seq data are deposited in the Genome Expression Omnibus under accession number GSE86619. This study was supported by Intramural grants from A*STAR to L.G.N.; BES-2013–065550 to J.M.A., BES-2010-032828 to M.C-A and JCI-2012-14147 to L.A.W (all from Ministerio de Economía, Industria y Competitividad; MEIC). SAF2014-61993-EXP to C.L-R., SAF2015-68632-R to M.A.M., SAF-2013-42920R and SAF2016-79040R (all from MEIC), 635122-PROCROP H2020 from the European Commission and ERC CoG 725091 from the European Research Council (ERC) to D.S. ERC AdG 692511 PROVASC from the ERC and SFB1123-A1 from the Deutsche Forschungsgemeinschaft to C.W.; MHA VD1.2/81Z1600212 from the German Center for Cardiovascular Research (DZHK) to C.W. and O.S.; SFB1123-A6 to O.S. and SFB914-B08 to O.S. and C.W.; INST 211/604-2, ZA 428/12-1, and ZA 428/13-1 to A.Z. PI12/00494 from Fondo

de Investigaciones Sanitarias (FIS) to C.M. PI13/01979, Cardiovascular Network grant RD 12/0042/0054 and CIBERCV to B.I.; SAF2015-65607-R, SAF2013-49662-EXP and PCIN-2014-103 from MEIC, and co-funding by Fondo Europeo de Desarrollo Regional (FEDER) to A.H. The CNIC is supported by the MEIC and the Pro CNIC Foundation, and is a Severo Ochoa Center of Excellence (MEIC award SEV-2015-0505). The authors declare no conflicts of interest.

References

Auffray, C., Fogg, D., Garfa, M., Elain, G., Join-Lambert, O., Kayal, S., Sarnacki, S., Cumano, A., Lauvau, G., and Geissmann, F. (2007). Monitoring of blood vessels and tissues by a population of monocytes with patrolling behavior. Science (New York, NY) *317*, 666-670.

Balabanian, K., Brotin, E., Biajoux, V., Bouchet-Delbos, L., Lainey, E., Fenneteau, O., Bonnet, D., Fiette, L., Emilie, D., and Bachelerie, F. (2012). Proper desensitization of CXCR4 is required for lymphocyte development and peripheral compartmentalization in mice. Blood *119*, 5722-5730.

Casanova-Acebes, M., Nicolas-Avila, J.A., Li, J.L., Garcia-Silva, S., Balachander, A., Rubio-Ponce, A., Weiss, L.A., Adrover, J.M., Burrows, K., N, A.G., *et al.* (2018). Neutrophils instruct homeostatic and pathological states in naive tissues. The Journal of experimental medicine *215*, 2778-2795.

Casanova-Acebes, M., Pitaval, C., Weiss, L.A., Nombela-Arrieta, C., Chevre, R., N, A.G., Kunisaki, Y., Zhang, D., van Rooijen, N., Silberstein, L.E., *et al.* (2013). Rhythmic modulation of the hematopoietic niche through neutrophil clearance. Cell *153*, 1025-1035.

Cuartero, M.I., Ballesteros, I., Moraga, A., Nombela, F., Vivancos, J., Hamilton, J.A., Corbi, A.L., Lizasoain, I., and Moro, M.A. (2013). N2 neutrophils, novel players in brain inflammation after stroke: modulation by the PPARgamma agonist rosiglitazone. Stroke; a journal of cerebral circulation *44*, 3498-3508.

Devi, S., Wang, Y., Chew, W.K., Lima, R., N, A.G., Mattar, C.N., Chong, S.Z., Schlitzer, A., Bakocevic, N., Chew, S., *et al.* (2013). Neutrophil mobilization via plerixafor-mediated CXCR4 inhibition arises from lung demargination and blockade of neutrophil homing to the bone marrow. The Journal of experimental medicine *210*, 2321-2336.

Druzd, D., Matveeva, O., Ince, L., Harrison, U., He, W., Schmal, C., Herzel, H., Tsang, A.H., Kawakami, N., Leliavski, A., *et al.* (2017). Lymphocyte Circadian Clocks Control Lymph Node Trafficking and Adaptive Immune Responses. Immunity *46*, 120-132.

Eash, K.J., Greenbaum, A.M., Gopalan, P.K., and Link, D.C. (2010). CXCR2 and CXCR4 antagonistically regulate neutrophil trafficking from murine bone marrow. The Journal of clinical investigation *120*, 2423-2431.

Eash, K.J., Means, J.M., White, D.W., and Link, D.C. (2009). CXCR4 is a key regulator of neutrophil release from the bone marrow under basal and stress granulopoiesis conditions. Blood *113*, 4711-4719.

Erlandsen, S.L., Hasslen, S.R., and Nelson, R.D. (1993). Detection and spatial distribution of the beta 2 integrin (Mac-1) and L-selectin (LECAM-1) adherence receptors on human neutrophils by high-resolution field emission SEM. J Histochem Cytochem *41*, 327-333.

Faust, N., Varas, F., Kelly, L.M., Heck, S., and Graf, T. (2000). Insertion of enhanced green fluorescent protein into the lysozyme gene creates mice with green fluorescent granulocytes and macrophages. Blood *96*, 719-726.

Finger, E.B., Bruehl, R.E., Bainton, D.F., and Springer, T.A. (1996). A differential role for cell shape in neutrophil tethering and rolling on endothelial selectins under flow. Journal of immunology (Baltimore, Md : 1950) *157*, 5085-5096.

Frenette, P.S., Mayadas, T.N., Rayburn, H., Hynes, R.O., and Wagner, D.D. (1996). Susceptibility to infection and altered hematopoiesis in mice deficient in both P- and E-selectins. Cell *84*, 563-574.

Fuchs, T.A., Brill, A., Duerschmied, D., Schatzberg, D., Monestier, M., Myers, D.D., Jr., Wrobleski, S.K., Wakefield, T.W., Hartwig, J.H., and Wagner, D.D. (2010). Extracellular DNA traps promote thrombosis. Proceedings of the National Academy of Sciences of the United States of America *107*, 15880-15885.

Garcia-Prieto, J., Villena-Gutierrez, R., Gomez, M., Bernardo, E., Pun-Garcia, A., Garcia-Lunar, I., Crainiciuc, G., Fernandez-Jimenez, R., Sreeramkumar, V., Bourio-Martinez, R.*, et al.* (2017). Neutrophil stunning by metoprolol reduces infarct size. Nature communications *8*, 14780.

Harbort, C.J., Soeiro-Pereira, P.V., von Bernuth, H., Kaindl, A.M., Costa-Carvalho, B.T., Condino-Neto, A., Reichenbach, J., Roesler, J., Zychlinsky, A., and Amulic, B. (2015). Neutrophil oxidative burst activates ATM to regulate cytokine production and apoptosis. Blood *126*, 2842-2851.

Hasenberg, A., Hasenberg, M., Mann, L., Neumann, F., Borkenstein, L., Stecher, M., Kraus, A., Engel, D.R., Klingberg, A., Seddigh, P.*, et al.* (2015). Catchup: a mouse model for imaging-based tracking and modulation of neutrophil granulocytes. Nature methods *12*, 445-452.

Hidalgo, A., Chang, J., Jang, J.E., Peired, A.J., Chiang, E.Y., and Frenette, P.S. (2009). Heterotypic interactions enabled by polarized neutrophil microdomains mediate thromboinflammatory injury. Nature medicine *15*, 384-391.

Hidalgo, A., Peired, A.J., Wild, M.K., Vestweber, D., and Frenette, P.S. (2007). Complete identification of E-selectin ligands on neutrophils reveals distinct functions of PSGL-1, ESL-1, and CD44. Immunity *26*, 477-489.

Janich, P., Pascual, G., Merlos-Suarez, A., Batlle, E., Ripperger, J., Albrecht, U., Cheng, H.Y., Obrietan, K., Di Croce, L., and Benitah, S.A. (2011). The circadian molecular clock creates epidermal stem cell heterogeneity. Nature *480*, 209-214.

Ley, K., Laudanna, C., Cybulsky, M.I., and Nourshargh, S. (2007). Getting to the site of inflammation: the leukocyte adhesion cascade updated. Nature reviews Immunology *7*, 678-689.

Li, B., and Dewey, C.N. (2011). RSEM: accurate transcript quantification from RNA-Seq data with or without a reference genome. BMC bioinformatics *12*, 323.

Li, J.L., Lim, C.H., Tay, F.W., Goh, C.C., Devi, S., Malleret, B., Lee, B., Bakocevic, N., Chong, S.Z., Evrard, M.*, et al.* (2016). Neutrophils Self-Regulate Immune Complex-Mediated Cutaneous Inflammation through CXCL2. The Journal of investigative dermatology *136*, 416-424.

Lionakis, M.S., Lim, J.K., Lee, C.C., and Murphy, P.M. (2011). Organ-specific innate immune responses in a mouse model of invasive candidiasis. Journal of innate immunity *3*, 180-199.

Man, K., Loudon, A., and Chawla, A. (2016). Immunity around the clock. Science (New York, NY) *354*, 999-1003.

Martin, C., Burdon, P.C., Bridger, G., Gutierrez-Ramos, J.C., Williams, T.J., and Rankin, S.M. (2003). Chemokines acting via CXCR2 and CXCR4 control the release of neutrophils from the bone marrow and their return following senescence. Immunity *19*, 583-593.

Mei, J., Liu, Y., Dai, N., Hoffmann, C., Hudock, K.M., Zhang, P., Guttentag, S.H., Kolls, J.K., Oliver, P.M., Bushman, F.D.*, et al.* (2012). Cxcr2 and Cxcl5 regulate the IL-17/G-CSF axis and neutrophil homeostasis in mice. The Journal of clinical investigation *122*, 974-986.

Muller, J.E., Tofler, G.H., and Stone, P.H. (1989). Circadian variation and triggers of onset of acute cardiovascular disease. Circulation *79*, 733-743.

Nguyen, K.D., Fentress, S.J., Qiu, Y., Yun, K., Cox, J.S., and Chawla, A. (2013). Circadian gene Bmal1 regulates diurnal oscillations of Ly6C(hi) inflammatory monocytes. Science (New York, NY) *341*, 1483-1488.

Nicolas-Avila, J.A., Adrover, J.M., and Hidalgo, A. (2017). Neutrophils in Homeostasis, Immunity, and Cancer. Immunity *46*, 15-28.

Nie, Y., Waite, J., Brewer, F., Sunshine, M.J., Littman, D.R., and Zou, Y.R. (2004). The role of CXCR4 in maintaining peripheral B cell compartments and humoral immunity. The Journal of experimental medicine *200*, 1145-1156.

Passegue, E., Wagner, E.F., and Weissman, I.L. (2004). JunB deficiency leads to a myeloproliferative disorder arising from hematopoietic stem cells. Cell *119*, 431-443.

Radu, M., and Chernoff, J. (2013). An in vivo assay to test blood vessel permeability. J Vis Exp, e50062.

Rittirsch, D., Huber-Lang, M.S., Flierl, M.A., and Ward, P.A. (2009). Immunodesign of experimental sepsis by cecal ligation and puncture. Nature protocols *4*, 31-36.

Robinson, M.D., McCarthy, D.J., and Smyth, G.K. (2010). edgeR: a Bioconductor package for differential expression analysis of digital gene expression data. Bioinformatics *26*, 139-140.

Schageman, J., Zeringer, E., Li, M., Barta, T., Lea, K., Gu, J., Magdaleno, S., Setterquist, R., and Vlassov, A.V. (2013). The complete exosome workflow solution: from isolation to characterization of RNA cargo. BioMed research international *2013*, 253957.

Scheiermann, C., Kunisaki, Y., and Frenette, P.S. (2013). Circadian control of the immune system. Nature reviews Immunology *13*, 190-198.

Scheiermann, C., Kunisaki, Y., Lucas, D., Chow, A., Jang, J.E., Zhang, D., Hashimoto, D., Merad, M., and Frenette, P.S. (2012). Adrenergic nerves govern circadian leukocyte recruitment to tissues. Immunity *37*, 290-301.

Schindelin, J., Rueden, C.T., Hiner, M.C., and Eliceiri, K.W. (2015). The ImageJ ecosystem: An open platform for biomedical image analysis. Mol Reprod Dev *82*, 518-529.

Schloss, M.J., Horckmans, M., Nitz, K., Duchene, J., Drechsler, M., Bidzhekov, K., Scheiermann, C., Weber, C., Soehnlein, O., and Steffens, S. (2016). The time-of-day of myocardial infarction onset affects healing through oscillations in cardiac neutrophil recruitment. EMBO molecular medicine *8*, 937-948.

Silver, A.C., Arjona, A., Walker, W.E., and Fikrig, E. (2012). The circadian clock controls toll-like receptor 9-mediated innate and adaptive immunity. Immunity *36*, 251-261.

Silvestre-Roig, C., Hidalgo, A., and Soehnlein, O. (2016). Neutrophil heterogeneity: implications for homeostasis and pathogenesis. Blood *127*, 2173-2181.

Simon, S.I., Nyunt, T., Florine-Casteel, K., Ritchie, K., Ting-Beall, H.P., Evans, E., and Needham, D. (2007). Dynamics of neutrophil membrane compliance and microstructure probed with a micropipet-based piconewton force transducer. Annals of biomedical engineering *35*, 595-604.

Sreeramkumar, V., Adrover, J.M., Ballesteros, I., Cuartero, M.I., Rossaint, J., Bilbao, I., Nacher, M., Pitaval, C., Radovanovic, I., Fukui, Y*., et al.* (2014). Neutrophils scan for activated platelets to initiate inflammation. Science (New York, NY) *346*, 1234-1238.

Sturn, A., Quackenbush, J., and Trajanoski, Z. (2002). Genesis: cluster analysis of microarray data. Bioinformatics *18*, 207-208.

Summers, C., Rankin, S.M., Condliffe, A.M., Singh, N., Peters, A.M., and Chilvers, E.R. (2010). Neutrophil kinetics in health and disease. Trends in immunology *31*, 318-324.

Tanji-Matsuba, K., van Eeden, S.F., Saito, Y., Okazawa, M., Klut, M.E., Hayashi, S., and Hogg, J.C. (1998). Functional changes in aging polymorphonuclear leukocytes. Circulation *97*, 91-98.

Tognini, P., Thaiss, C.A., Elinav, E., and Sassone-Corsi, P. (2017). Circadian Coordination of Antimicrobial Responses. Cell host & microbe *22*, 185-192.

Uhl, B., Vadlau, Y., Zuchtriegel, G., Nekolla, K., Sharaf, K., Gaertner, F., Massberg, S., Krombach, F., and Reichel, C.A. (2016). Aged neutrophils contribute to the first line of defense in the acute inflammatory response. Blood.

Vinten-Johansen, J. (2004). Involvement of neutrophils in the pathogenesis of lethal myocardial reperfusion injury. Cardiovascular research *61*, 481-497.

Vintersten, K., Monetti, C., Gertsenstein, M., Zhang, P., Laszlo, L., Biechele, S., and Nagy, A. (2004). Mouse in red: red fluorescent protein expression in mouse ES cells, embryos, and adult animals. Genesis *40*, 241-246.

von Andrian, U.H., Hasslen, S.R., Nelson, R.D., Erlandsen, S.L., and Butcher, E.C. (1995). A central role for microvillous receptor presentation in leukocyte adhesion under flow. Cell *82*, 989-999.

Yu, X., Rollins, D., Ruhn, K.A., Stubblefield, J.J., Green, C.B., Kashiwada, M., Rothman, P.B., Takahashi, J.S., and Hooper, L.V. (2013). TH17 cell differentiation is regulated by the circadian clock. Science (New York, NY) *342*, 727-730.

Zarbock, A., Lowell, C.A., and Ley, K. (2007). Spleen tyrosine kinase Syk is necessary for E-selectin-induced alpha(L)beta(2) integrin-mediated rolling on intercellular adhesion molecule-1. Immunity *26*, 773-783.

Zhang, D., Chen, G., Manwani, D., Mortha, A., Xu, C., Faith, J.J., Burk, R.D., Kunisaki, Y., Jang, J.E., Scheiermann, C*., et al.* (2015). Neutrophil ageing is regulated by the microbiome. Nature *525*, 528-532.

Figure legends

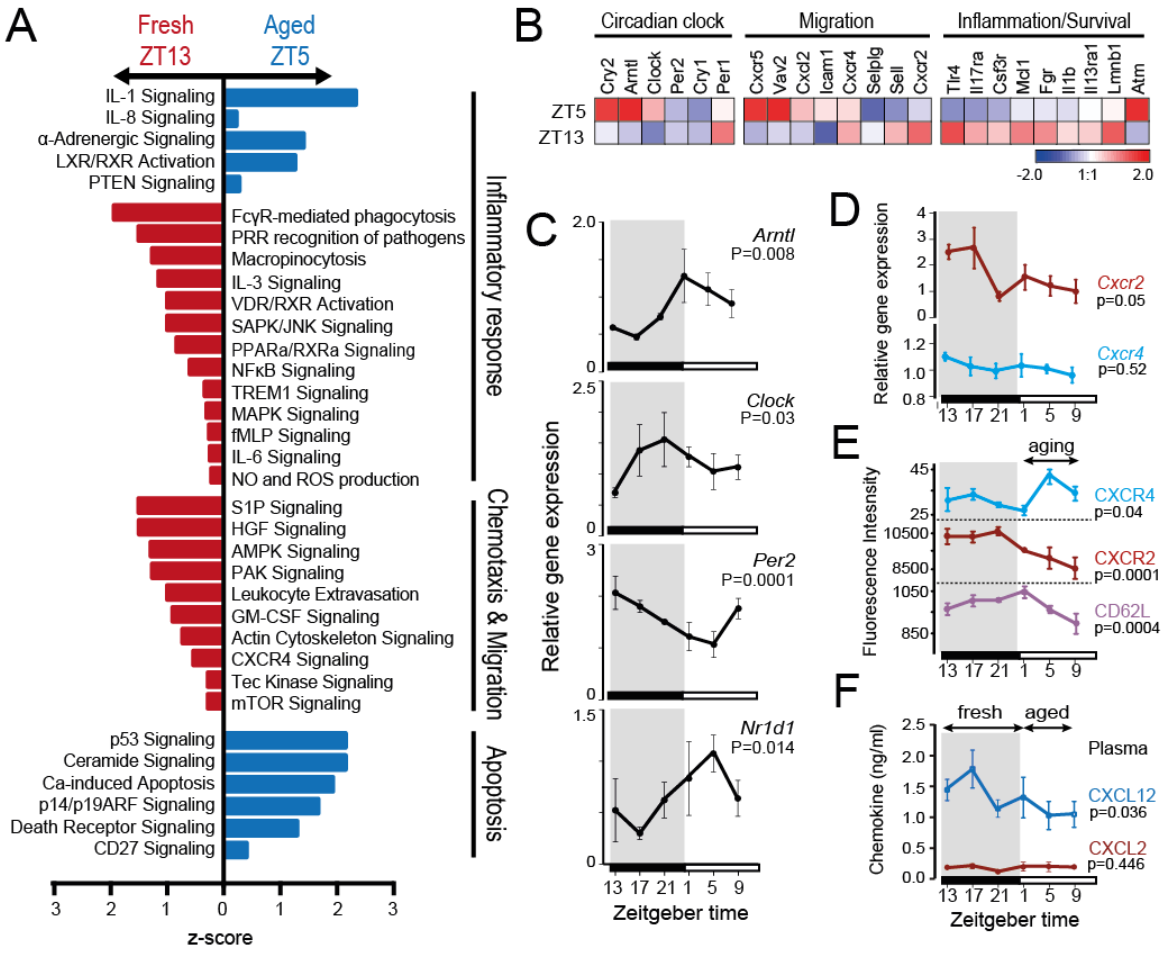

Figure 1. Cell-intrinsic rhythms in circulating neutrophils. See also Figure S1.
(A) Molecular pathways differentially regulated in circulating wild-type neutrophils at ZT5 vs. ZT13. Comparisons are presented as z-score values.
(B) Heat map of selected genes at ZT5 vs ZT13, including genes of the circadian clock and genes encoding proteins related to migration and inflammation. The color scale indicates fold changes of expression for each gene.
(C) Diurnal expression of the indicated clock genes in neutrophils isolated from the circulation of wild-type mice at the indicated zeitgeber times. Shaded areas represent night; n=2-6 mice per time point.
(D) Diurnal expression of *Cxcr2* and *Cxcr4* in circulating wild-type neutrophils at the indicated times; n=2-6 mice per time point. The diurnal curves are repeated (dashed lines) to better appreciate the pattern.
(E) Surface levels of CXCR4, CXCR2 and CD62L at different diurnal times measured by flow cytometry; n=5 mice. Highlighted is the time of aging (ZT1 to ZT9), when CD62L and CXCR2 levels go down and CXCR4 goes up. The diurnal curves are repeated (dashed lines) to better appreciate the pattern.
(F) Diurnal levels of CXCL2 and CXCL12 in the plasma of wild-type mice; n=5-10 mice per time point. The diurnal curves are repeated (dashed lines) to better appreciate the pattern.
All values are presented as mean ± SEM. P values were determined by amplitude vs. zero t-test analyses (see Statistical methods) to test for circadian behavior (C-F).

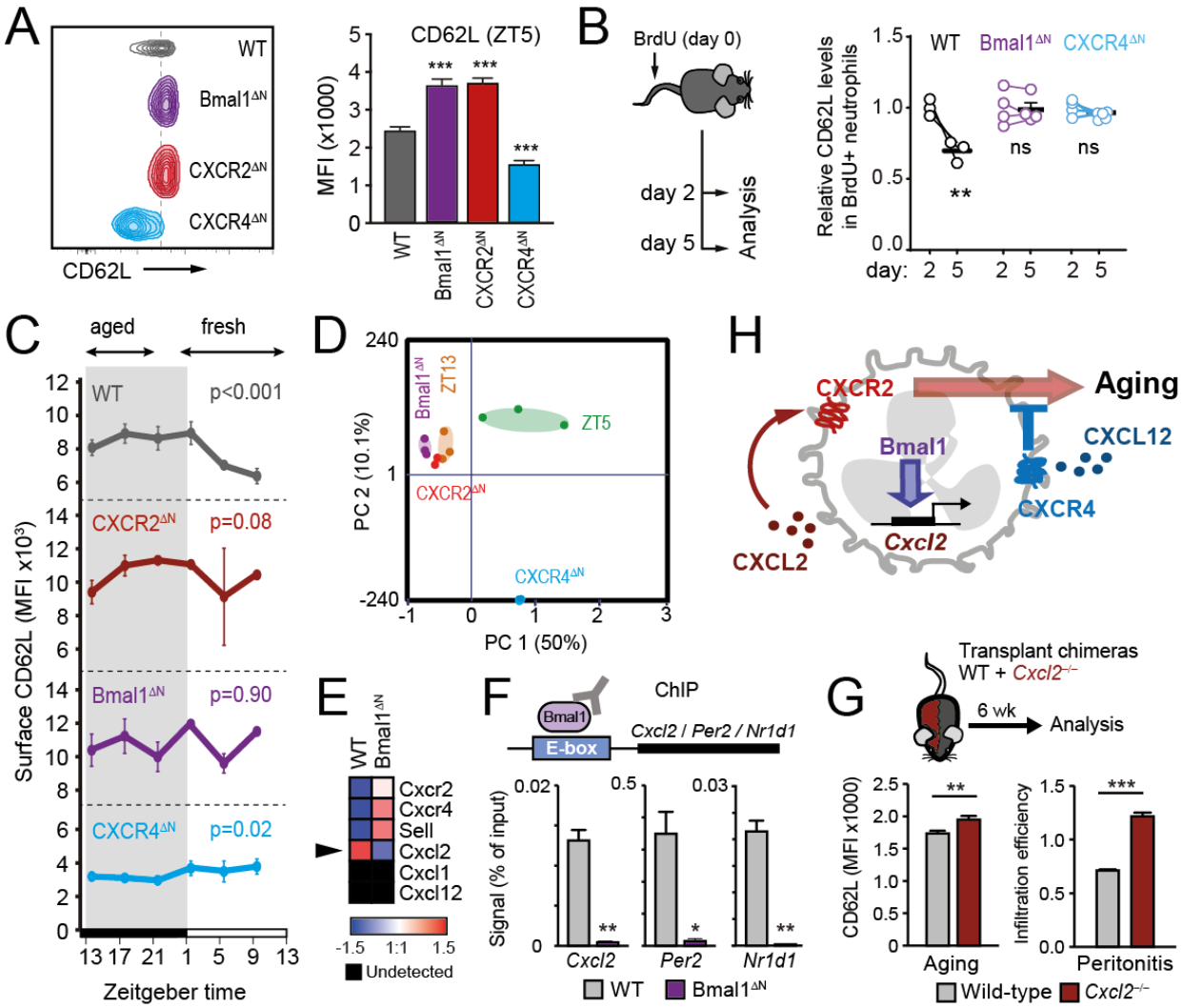

Figure 2. Bma1, CXCR2 and CXCR4 form a diurnal clock in neutrophils. See also Figure S2.
(A) Surface expression of CD62L in wild-type and mutant neutrophils at ZT5. Cytometric data was obtained from transplant chimeras of wild-type with each mutant. Bars at right show median fluorescence intensity; n=14-30 mice per group.
(B) In vivo BrdU labeling of neutrophils followed by analysis of CD62L in BrdU+ cells 2 and 5 days after injection. Note that as labeled neutrophils enter the bloodstream, they lose CD62L over time in WT mice, but not in Bmal1$^{\Delta N}$ and CXCR4$^{\Delta N}$ mutants. Data is normalized to day 2 levels in each group; n=3-5 mice per group.
(C) Diurnal levels of CD62L in circulating neutrophils in wild-type and mutant mice, as determined by flow cytometry. The times when neutrophils are phenotypically fresh or aged are indicated on top; n=3-10 mice per time point. P values were determined by amplitude vs. zero t-test analyses.
(D) Principal component analyses of differentially expressed genes in circulating neutrophils from wild-type neutrophils at ZT5 and ZT13, and Bmal1$^{\Delta N}$, CXCR2$^{\Delta N}$ and CXCR4$^{\Delta N}$ mutants at ZT5.
(E-G) Bmal1-regulated expression of CXCL2 controls aging. (E) Heat-map showing differential expression of aging-related genes in wild-type and Bmal1$^{\Delta N}$ neutrophils. Expression of Cxcl1 and Cxcl12 was undetectable. Data are from triplicate samples of each group obtained at ZT5. (F) Experimental design and ChIP analyses of Bmal1 binding to E-box-containing promoter regions

of *Cxcl2*, *Per2* and *Nr1d1* in wild-type and Bmal1$^{\Delta N}$ neutrophils.(G) Experimental setup and phenotype of Cxcl2$^{-/-}$ neutrophils in transplantation chimeras. *Cxcl2*$^{-/-}$ neutrophils display elevated CD62L expression and enhanced migration to zymosan-treated peritoneum, both of which are consistent with disrupted aging.
(H) Model of neutrophil aging: CXCR2 signaling drives aging, while CXCR4 antagonizes these signals and prevents it. Bmal1 regulates *Cxcl2* expression to promote autocrine CXCR2 signaling and aging.
Except where indicated, all values are mean ± SEM. **; $p<0.01$; ***, $p<0.001$ as determined by one-way ANOVA (A), upaired t-test (B, F) or paired t-test (D, G).

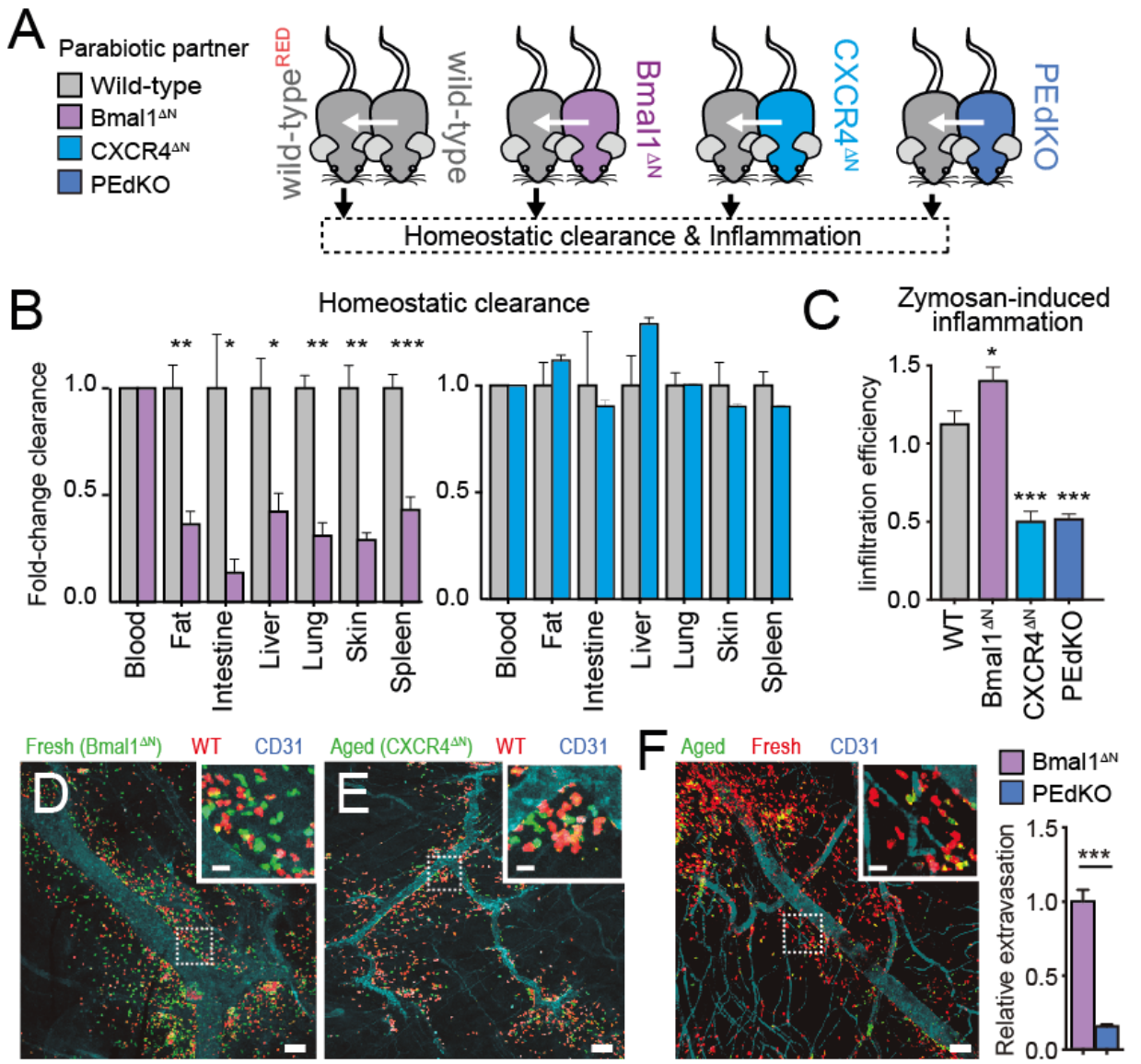

Figure 3. Diurnal aging impairs inflammatory recruitment but favors homeostatic clearance. See also Figure S3.

(A) Experimental setup to test homeostatic or inflammatory recruitment in the indicated parabiotic pairs. Mutant neutrophils that enter tissues of their wild-type^{RED} partners (expressing DsRed) allowed estimation of their migratory capacity relative to wild-type cells.

(B) Quantification of Bmal1$^{\Delta N}$ (left) and CXCR4$^{\Delta N}$ (right) neutrophils cleared in multiple tissues of wild-type partners at ZT5; values are adjusted to ratios in blood and normalized to wild-type neutrophils cleared in wild-type partners; n=3-8 mice.

(C) Quantification of control and mutant neutrophils that infiltrate the inflamed peritoneum of wild-type parabiotic partners at ZT5; n=3-5 mice.

(D-E) Whole-mount staining of TNFα-treated cremaster muscles from transplant chimeras of wild-type and Bmal1$^{\Delta N}$ donors (D) or wild-type and CXCR4$^{\Delta N}$ donors (E), showing extravasated neutrophils and vessels. Extravasated neutrophils from each partner are quantified in Fig.4B (Extravasation).

(F) Whole-mount staining as in (D), comparing constitutively fresh and aged neutrophils in Bmal1$^{\Delta N}$ mice (fresh; red) set in parabiosis with PEdKO^{GFP} (aged; green) partners. The relative infiltration of each partner is quantified in the right bar-graph. Scale bars for (D-F), 70 μm. Insets show details of the differential infiltration of the two types of neutrophils in each experiment; scale bars, 10 μm.

All bars show mean ± SEM. *, $p<0.05$; **; $p<0.01$; ***, $p<0.001$ as determined by unpaired (B) or paired (C, F) t-test analysis.

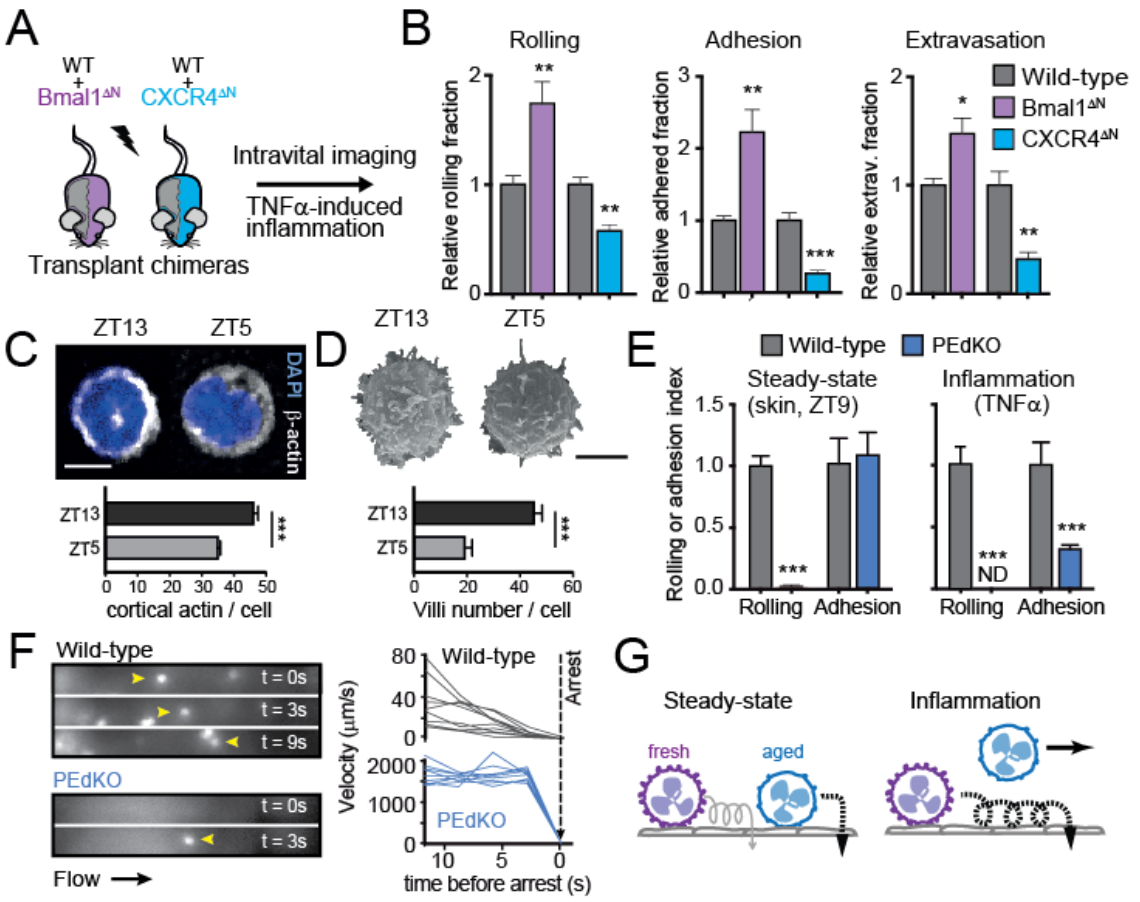

Figure 4. Microvilli collapse and impaired rolling are hallmarks of aged neutrophils. See also Figure S4.

(A) Strategy for competitive recruitment of neutrophils to inflamed tissues using bone marrow chimeras, at ZT5.

(B) Relative frequencies of rolling, adherent and extravasated fresh (Bmal1$^{\Delta N}$) and aged (CXCR4$^{\Delta N}$) neutrophils, normalized to wild-type controls in chimeric mice; n=30-61 venules from 5-6 mice.

(C) Immunofluoresence staining of β-actin in wild-type neutrophils at ZT5 and ZT13, and frequency of neutrophils with cortical distribution of actin; n=324-330 cells per group.

(D) Scanning electron micrographs of wild-type neutrophils at ZT5 and ZT13, and quantification of the number of villi on their surface. Scale bar, 5 μm; n=23-29 cells per group.

(E) Rolling and adhesion of neutrophils on cremasteric venules after treatment with TNF-α (Inflammation), or on naïve dermal microvessels at ZT9-13 (Steady-state) in wild-type or PEdKO mice. n=50-55 venules from 4-5 mice (steady-state), and 25-27 venules from 3-5 mice (inflamed cremaster). ND, none detected.

(F) Kinetics of neutrophils (Ly6G+; yellow arrows) prior firm arrest on dermal microvessels in the steady-state. Left, sequential intravital frames of the same vessels of wild-type or PEdKO mice with neutrophils arresting in the last sequence (reverse arrows). Right, flow/roll dynamics of neutrophils before firm arrest; n=10 cells shown per group.

(G) Model for the preferential recruitment of fresh and aged neutrophils into inflamed or naïve tissues, respectively.

Bars show mean ± SEM. *, p<0.05; **; p<0.01; ***, p<0.001 as determined by paired (B), or unpaired t-test analysis (C-D), or non-parametric Mann-Whitney test (E).

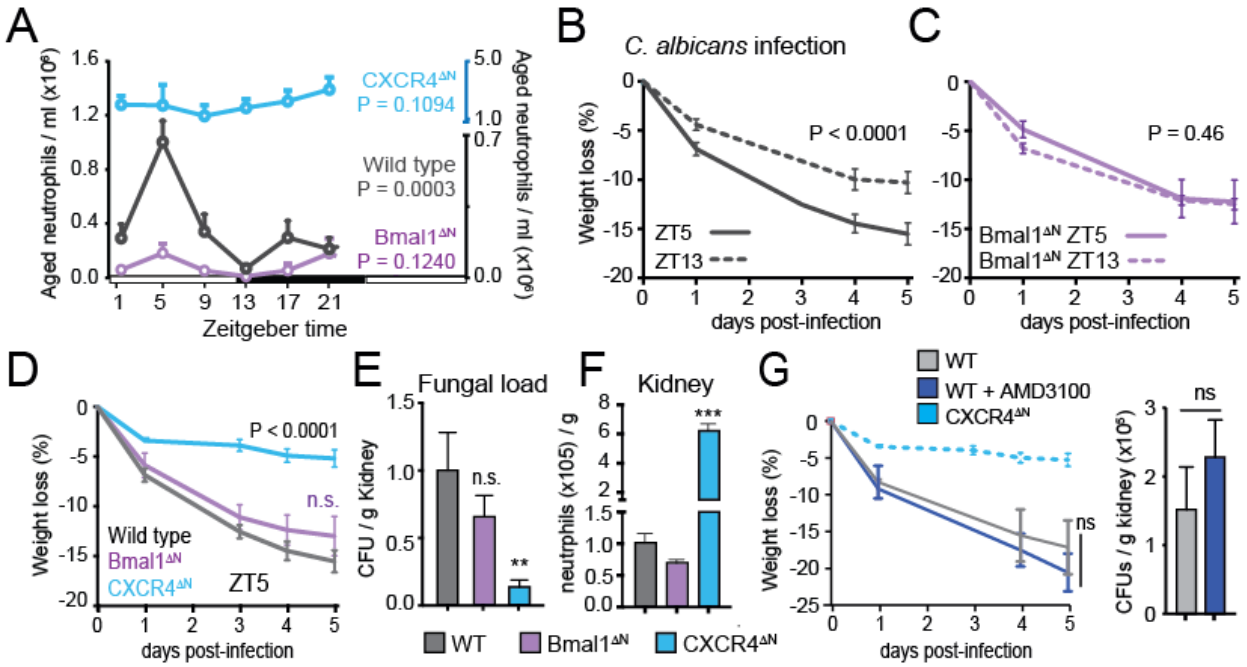

Figure 5. Neutrophil aging confers diurnal protection against infection. See also Figure S5.
(A) Diurnal numbers of CD62L^{LO} aged neutrophils in the blood of wild-type, Bmal1$^{\Delta N}$ and CXCR4$^{\Delta N}$ mice; n = 3-6 mice. See also Figure S5A.
(B-C) Weight loss kinetics of wild-type (B) and Bmal1$^{\Delta N}$ mice (C) infected with *C. albicans* at ZT5 or ZT13; n=5-21 mice per time point.
(D) Weight loss curves comparing wild-type, Bmal1$^{\Delta N}$ and CXCR4$^{\Delta N}$ mice infected at ZT5; n=12-14 mice.
(E) Fungal burden at day 5 in the kidneys from the mice in (D), normalized to WT.
(F) Number of neutrophils in the kidneys of non-infected mice; n=4 mice per group.
(G) Kinetics of weight-loss in control- or AMD-treated wild-type mice after systemic *C. albicans* infection at ZT5. The dashed line show weight loss in CXCR4$^{\Delta N}$ mice shown in Fig.4D for reference. Bars at right show fungal burden in kidneys at day 5 post-infection; n=10 mice
Data are shown as mean ± SEM. **; p<0.01; ***, p<0.001; n.s., not significant, as determined by amplitude vs. zero t-test (A), two-way ANOVA (B-D.G), one-way ANOVA with Dunnett's multigroup correction (E-F), and unpaired t-test analysis (G).

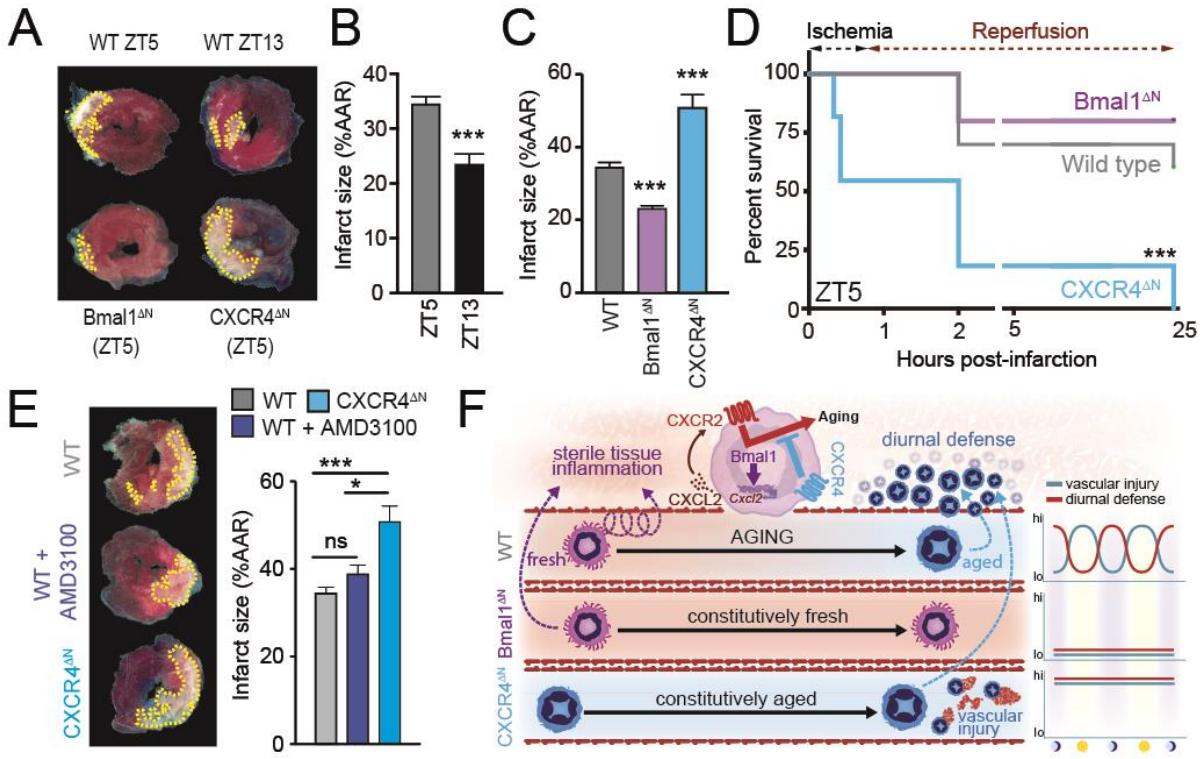

Figure 6. Aged neutrophils aggravate myocardial infarction. See also Figure S6.
(A) Representative images showing infarcted areas of hearts from wild-type mice subjected to transient occlusion of the coronary artery followed by 1 hour reperfusion at ZT5 or ZT13, or in the indicated mutant mice at ZT5. Dotted yellow lines highlight areas of dead myocardium; n=4-8 mice per group.
(B) Quantification of infarct sizes for wild-type mice at different diurnal times, after correction for areas at risk (AAR; see related Figure S5); n=5-8 mice.
(C) Quantification of infarct sizes in wild-type, Bmal1$^{\Delta N}$ and CXCR4$^{\Delta N}$ mice at ZT5, after correction for AAR (see related Figure S5); n=4-8 mice.
(D) Survival curves of wild-type, Bmal1$^{\Delta N}$ and CXCR4$^{\Delta N}$ mice subjected to myocardial infarction at ZT5; n=9-11 mice.
(E) Representative images showing infarcted areas of hearts from untreated or AMD3100-treated wild-type mice, and CXCR4$^{\Delta N}$ mice. Surgeries were performed at ZT5 and dead myocardium is highlighted as in (A). Bars at right show quantification of infarcted areas in the same groups; n=4-5 mice.
Bars show mean ± SEM. *; p<0.05; ***, p<0.001; n.s., not significant, as determined by one-way ANOVA with Dunnett's multigroup correction (C, E), unpaired t-test analysis (B), and Log-rank test (D)
(F) Summary of molecular events regulating neutrophil aging, and the consequence of deleting regulators of aging (Bmal1 and CXCR4) in the dynamics and strength of diurnal defense and vascular injury. Defective aging (Bmal1$^{\Delta N}$) impairs the evening boost in anti-microbial defense but protects from vascular injury, whereas constitutive aging (CXCR4$^{\Delta N}$) enhances the response to infections at the cost of exacerbated thrombo-inflammation.

STAR*METHODS

CONTACT FOR REAGENT AND RESOURCE SHARING

Reagents used in this study are readily available from the noted commercial suppliers in the method itself. Further information and requests for other resources and reagents should be directed to and will be fulfilled by the Lead Contact: Andrés Hidalgo (ahidalgo@cnic.es)

EXPERIMENTAL MODEL AND SUBJECT DETAILS

Mice

All experiments were performed in 7 to 18 week-old male C57BL/6 mice kept in a specific pathogen-free facility at Centro Nacional de Investigaciones Cardiovasculares (CNIC) under a 12h light/12h dark schedule (lights on at 7am, off at 7pm), with water and chow available *ad libitum*. To generate mice with neutrophil-specific deficiency, we crossed *Arntl*$^{fl/fl}$ (kindly provided by S. Benitah) (Janich et al., 2011), *Cxcr4* $^{fl/fl}$ (Nie et al., 2004) or C*xcr2* $^{fl/f}$ *(Schloss et al., 2016)* with hMRP8^{CRE} mice (Passegue et al., 2004), *Cxcr4*^{WHIM} mice with a hyper-signalling form of CXCR4 have been described (Balabanian et al., 2012) and were used as donors to generate BM chimeras. *Cxcl2*$^{-/-}$ mice were obtained from Jackson. In some control experiments we crossed *Cxcr2*$^{fl/f}$ mice with the Ly6G^{CRE} mice (Hasenberg et al., 2015). Mice deficient in P an E-selectins (*Sele* and *Selp*; PEdKO) have been previously described (Frenette et al., 1996). To obtain reporter mice for intravital microscopy (IVM) studies, we crossed the PEdKO with transgenic mice expressing DsRed under the control of the β-actin promoter (DsRed^{Tg}; (Vintersten et al., 2004)) or with the *Lyz2*^{GFP} reporter mouse (PEdKO^{GFP} mice)(Faust et al., 2000). Both were also used in wild-type reporters for some intravital imaging experiments. In control experiments, we confirmed that wild-type mice used as controls yielded a similar phenotype compared with hMRP8^{CRE} alone, Arntl$^{fl/fl}$ and Cxcr4$^{fl/fl}$ mice (not shown). No specific randomization method was followed in this study. All experimental procedures were approved by the Animal Care and Ethics Committee of CNIC and the regional authorities.

Human studies

The study comprised blood from 12 healthy volunteers withdrawn at 12am, 4pm, 8pm, 12pm, 4am and 8am. The study complied with current Spanish legislation on clinical research in humans and was approved by the Ethics Committee for Clinical Research of Hospital Universitario de la Princesa. All volunteers gave written informed consent to participate in the study.

METHOD DETAILS

Analysis of human samples

Total blood obtained from 12 healthy volunteers at 12am, 4pm, 8pm, 12pm, 4am and 8am and erythrocytes lysed in hypotonic buffer. Cells were incubated in 100µl PBS buffer containing 2 mM EDTA and 1% BSA (PEB buffer) with the following antibodies: anti-CXCR4-allophycocianin (APC; clone 12G5), anti-CD11b-FITC (clone ICRF44; both from eBiosciences), anti-CD16-pacific blue (clone 3G8), anti-CD62L-phycoerythrin (PE; clone DREG56), anti-CD11c-APC and 7AAD (all

from BD Biosciences). Cells were washed and analysed in a Canto flow cytometer at the Hospital de la Princesa, Madrid.

Parabiosis

We followed previously published procedures (Casanova-Acebes et al., 2013). Briefly, anesthetized mice were shaved and matched incisions were made from the olecranon to the knee joint, then olecranon and knee were attached by a single suture from one mouse to the other, using 5-0 polypropylene, and the dorsal and ventral skins were stitched by continuous suture. Analyses were done 4 to 6 weeks after surgery.

Cytometry and cell sorting

Cytometric analyses were performed using a Sony SP6800 Spectral Analyzer (Sony Biotechnology, Japan) or a LSRII Fortessa. For human sample cytometry we used a Canto flow cytometer (BD BioSciences). All cell sorting experiments were performed using an FACS Aria cell sorter (BD Biosciences), except the circadian sorting of blood neutrophils for qPCR analysis, which was performed using a Sony SH800S Cell Sorter. In all cases we obtained purities > 95%. All analyses, except for human samples, were done at the Cellomics Unit of the CNIC. All antibodies and streptavidin conjugates used in this study are listed in Table S2.

Table S2. List of antibodies used in this study.

CXCR4-APC	12G5	Human	eBioscience
CD11b-FITC	ICRF44	Human	eBioscience
CD16-Pacific Blue	3G8	Human	BD
CD62L-PE	DREG56	Human	BD
CD11c-APC	B-ly6	Human	BD
Ly6G-AF647	1A8	Mouse	eBioscience
Ly6G-Dylight 450	1A8	Mouse	BioXcell (conjugated in-house)
Ly6G-Dylight 650	1A8	Mouse	BioXcell (conjugated in-house)
Ly6G-FITC	1A8	Mouse	eBioscience
CD45-PerCP-Cy5.5	30-F11	Mouse	Biolegend
CD11b-PE	M1/70	Mouse	Tonbo Biosciences
CD11b-FITC	M1/70	Mouse	BD
CXCR2-PerCP-Cy5.5	SA044G4	Mouse	Biolegend
CXCR4-APC	2B11	Mouse	eBioscience
CD41-PE	MWReg30	Mouse	eBioscience
Ly6C-FITC	HK1.4	Mouse	Biolegend
CD62L-APC	MEL-14	Mouse	eBioscience
CD62L-FITC	MEL-14	Mouse	eBioscience
CD11b-BV510	M1/70	Mouse	Biolegend
CD31-APC	390	Mouse	eBioscience
Ki-67-e660	SolA15	Mouse	Thermo Fisher

Whole mount staining of excised cremaster muscles

Excised cremaster muscles were fixed in 4% paraformaldehyde at 4ºC overnight. Fixed samples were washed 3 times in PBS containing 0.5% Triton-x 100 (PBST) and blocked for 2 h in PBST 25% FBS at room temperature with shaking. Staining of neutrophils was performed using a biotinylated anti-Mrp14 antibody (clone 2B10 kindly provided by Dr. N. Hogg, Cancer Research UK, London) and blood vessels with an anti-CD31 antibody (BD Biosciences) in 10% FBS-PBST overnight at 4ºC with shaking. Cremaster muscles were then washed and incubated with secondary antibody (goat anti-rabbit-Alexa 405 or –Alexa 647; Life Technologies) and Alexa-488 conjugated Streptavidin in 10%FBS-PBST for 4h at room temperature. Samples were then washed and mounted in Mowiol 4-88 (Mw 31,000; Sigma). Imaging of whole-mount intestines was performed using a Leica SP8 X confocal microscopy system coupled to a DMI6000 inverted microscope, with 10x (HC PL Fluotar 10x/0.3 Dry) or 63x (HC PL Apo CS2 63x/1.4 OIL) magnification objectives. For in-depth quantification, large Z-stack and panoramic-stitched images were taken with a Nikon A1R confocal system coupled to a Nikon Eclipse-Ti inverted microscope with the following lines: Diode 402nm Argon Laser 457, 476, 488, 514nm Diode 561nm HeNe Laser 642nm using a Plan Apo 10x/0,45 dry objective and the software NIS Elements AR 4.30.02 (Build 1053 LO, 64 bits, Nikon Instruments, Tokyo, Japan) for acquisition of confocal 3D tile-scan images of the whole cremaster muscle, which were afterwards analysed using Imaris (Bitplane, Zurich, Switzerland). All imaging was performed at the Microscopy & Dynamic Imaging Unit of CNIC.

RNA isolation, reverse transcription and rtPCR.

Total RNA was prepared with the RNA Extraction RNeasy Plus Mini-kit (QIAGEN) and RNA was reverse-transcribed with the High-Capacity cDNA Reverse Transcription kit (Applied Biosystems; Carlsbad, CA) according to the manufacturer's protocol. Real-time quantitative PCR (SYBR-green, Applied Biosystems) assays were performed with an Applied Biosystems 7900HT Fast Real-Time PCR System sequencer detector. Expression was normalized to the expression of the *36b4* housekeeping gene. Primer sequences are listed in the Table S3.

Chromatin immunoprecipitation (ChIP).

Neutrophils were sorted from the bone marrow as indicated previously and fixed in 0.75% formaldehyde for 10 min at room temperature. Formaldehyde was then quenched with glycine (final concentration 0.26 M) for 5 min. After washing twice with cold PBS, cells were pelleted and frozen at -80°C. Each sample was lysed in 0.25 ml of lysis buffer (1% SDS, 10 Mm EDTA, 50 mM Tris-HCl pH 8, 1 mM PMSF, 5 µg/ml leupeptin/aprotinin, 1 µg/ml pepstatin A, 10mM NaF, 10 mM sodium orthovanadate, and 10 mM β-glycerophosphate) for 30 min with rotation at room temperature. Lysates were sonicated using the Diagenode Bioruptor sonication system (Diagenode, Bioruptor UCD-200TM-EX). Each sample was sonicated for two rounds of six cycles (30s ON and 30s OFF) at the high power setting to obtain DNA fragments between 500 and 1000 bp. After sonication, samples were centrifuged to remove insoluble debris, supernatants were collected and 5% of each sample was separated to use as a measure of chromatin input for normalization. The rest of the sample was diluted 1/10 in ChIP dilution buffer (1% TritonX-100, 20 mM Tris-HCl, pH 8, 2 mM EDTA, 150 mM NaCl, 1 mM PMSF, 5 µg/ml leupeptin, 5 µg/ml aprotinin, 1 µg/ml pepstatin A, 10 mM NaF, 10 mM sodium orthovanadate, and 10 mM β-glycerophosphate) for immunoprecipitation. Samples were precleared with protein A Sepharose beads (GE

Healthcare, 17-0780-01) that were previously pre-adsorbed with fish sperm DNA (Roche, 11 467 140 001) and bovine serum albumin (New England Biolabs, Ref. B9001S) for 1 hour at 4°C. Anti-Bmal1 antibody (ChIP Grade (ab3350)) was added to the lysates after removing the preclearing beads and incubated overnight at 4°C. Pre-adsorbed protein A Sepharose beads were then added, incubated for 1 hour at 4°C, and then washed three times with ChIP washing buffer (0.1% SDS, 1% TX-100, 20 mM Tris-HCl, pH 8, 2 mM EDTA, and 150 mM NaCl) and once with final washing buffer (0.1% SDS, 1% TX-100, 20 mM Tris-HCl pH 8, 2 mM EDTA, and 500 mM NaCl). To elute DNA, beads were gently shaken with 200 µl elution buffer (1% SDS and 100 mM $NaHCO_3$) for 45 min at room temperature. To reverse the crosslinking, samples were incubated overnight at 65°C. Then samples were incubated with 3 µl RNase (Roche, 11119915001) 30 min at 37°C prior to the addition of 8 µl of Proteinase K (Roche, 3115828001) for 1 hour at 50°C and DNA was purified by ethanol precipitation. Immunoprecipitated chromatins and their respective inputs before immunoprecipitation were analyzed by RT-qPCR using the primers listed in Table S3. The primers for the Cxcl2, Per2 and Nr1d1 promoter regions were designed in the vicinity of E-box sequences.

Table S3. List of primers used for quantitative PCR and ChIP analyses.

Csf3r	**Forward**	**CTGATCTTCTTGCTACTCCCCA**
	Reverse	GGTGTAGTTCAAGTGAGGCAG
Il1b	Forward	AGTGAGGAGAATGACCTGTTC
	Reverse	CGAGATGCTGCTGTGAGATT
Sell	Forward	TACATTGCCCAAAAGCCCTTAT
	Reverse	CATCGTTCCATTTCCCAGAGTC
Cxcr4	Forward	TCAGTGGCTGACCTCCTCTT
	Reverse	CTTGGCCTTTGACTGTTGGT
Mcl1	Forward	AAAGGCGGCTGCATAAGTC
	Reverse	TGGCGGTATAGGTCGTCCTC
Cxcr2	Forward	TCTGGCATGCCCTCTATTCTG
	Reverse	AAGGTAACCTCCTTCACGTAT
Arntl	Forward	AGAGGCGTCGGGACAAAATGAACAG
	Reverse	AACAGCCATCCTTAGCACGGTGA
Clock	Forward	CCTATCCTACCTTGGCCACACA
	Reverse	TCCCGTGGAGCAACCTAGAT
Per2	Forward	CCATCCACAAGAAGATCCTAC
	Reverse	GCTCCACGGGTTGATGAAGC
Nr1d1	Forward	CTTCATCCTCCTCCTCCTTCTA
	Reverse	GTAATGTTGCTTGTGCCCTTG
36b4	Forward	ACTGGTCTAGGACCCGAGAAG
	Reverse	TCCCACCTTGTCTCCAGTCT
Cxcl2 (ChIP)	Forward	CCCAGTGTCTTCTCCTACAGG
	Reverse	GGCTATCCAGGGAGACACTC
Per2 (ChIP)	Forward	GGCACTCCGACCAATGGC
	Reverse	CGTCTGTCCCTTGCTCGG
Nr1d1 (ChIP)	Forward	ACACACTCTCTGCTCTTCCC
	Reverse	AGGTTGTGATGGCCTCTCTC

Intravital imaging of the mouse skin

For intravital microscopy of the dermal microcirculation, the dorsal side of the ear of anesthetized mice was mounted on a custom-built support, and we acquired images from several venules in 2 minute-long time-lapse videos at 3 s intervals. We used the VIVO system built by 3i (Intelligent Imaging Innovations, Dever, CO) upon an Axio Examiner Z.1 workstation (Zeiss, Oberkochen, Germany) and mounted on a 3D motorized stage (Sutter Instrument, Novato, CA). The system was equipped with a CoolLED pE widefield fluorescence LED light source (CoolLED Ltd. UK) and a quad pass filter cube with Semrock Di01-R405/488/561/635 dichroic and FF01-446/523/600/677 emitter. A plan-apochromat 40x W NA1.0 objective (Zeiss) was used and images were collected with a CoolSnap HQ2 camera (Photometrics, Tucson, AZ). The system was run on a Dell Precision T7500 computer system (Dell Inc., Round Rock, TX) using the SlideBook software (Intelligent Imaging Innovations). Acquisitions were made at ZT5, ZT9 or ZT13 and neutrophils were stained with an AF647-conjugated anti-Ly6G antibody (clone 1A8, BioXcell), while blood vessels were visualized using red fluorescent Dextran (Molecular Probes). In some groups, anti-P and E-selectin antibodies or Rat IgG control antibody (25 µg/mouse) were injected 2h before imaging. Quantification was done using the ImageJ (NIH, Bethesda, MD). Cells were considered adhered if they remained stationary on the venule for over 30 seconds. Vessel diameters were measured using the ImageJ software (Schindelin et al., 2015) to normalize the number of adherent cells.

Intravital microscopy of the cremaster muscle

Intravital microscopy of the cremaster muscle after TNFα stimulation (R&D Systems, 0.5µg intrascrotal injection) was performed as previously reported(Hidalgo et al., 2009) using the VIVO system indicated above. For confocal IVM, we used laser stacks for 488, 561 and 640nm beams coupled with a confocal scanner (Yokogawa CSUX-A1; Yokogawa, Japan) and images were acquired with 0.5µm Z-intervals. The SlideBook software was used for acquisition and analysis. Ten to twenty venules segments per mouse were analysed 150 to 210 min after TNF-α treatment in multiple fluorescence channels (Cy3/561 for PE, FITC/488 for FITC and Cy5/640 for APC) and bright-field images with 1x1 or 2×2 binning with 3 second interval for 2 min on each field of view. For double staining with PE- and FITC-conjugated antibodies, acquisition was facilitated in single (FITC) and quadrant (PE) filters in order to avoid bleed-through of fluorescent signals between channels. For the visualization of leukocytes, fluorescently labelled anti-Ly6G-APC, anti-Ly6C-FITC and anti-CD62L-APC antibodies were injected intravenously at 1 µg/mouse.

For analysis of rolling and adhered cells to the inflamed endothelium we used the SlideBook software. Counts of rolling or adhered cells in 2 minute captures (captured at 3 second intervals) were normalized using the width of the vessel to allow comparison among all vessels. For adhesion or rolling efficiency indices, this data was compared with the frequency of free-flowing WT and experimental cells in the blood for each mouse, which was obtained from cytometric analysis of blood neutrophils for each parabiont or BM chimeric mouse. Kinetic parameters for crawling neutrophils were calculated using ImageJ, with the help of the Manual Tracking plugin (Fabrice Cordelières, Institut Curie, France) and the Chemotaxis and Migration Tool (Gerhard Trapp and Elias Horn, ibidi GmbH, Germany). Analyses of extravasated neutrophil were performed on large tile-scans of whole-mounted cremaster muscles with Imaris (Bitplane AG,

Switzerland). We performed blind automatic counting of extravasated neutrophils by masking out the vessels using $CD31^+$ fluorescence (on the BMT WT:$Bmal1^{\Delta N}$, WT:$CXCR4^{\Delta N}$ chimeras and PEdKO:$Bmal1^{\Delta N}$ parabionts) or manually delimiting the vessels using brightfield or laminin fluorescence (on PEdKO-WT parabionts). Kinetic parameters for extravasated neutrophils were obtained in the $DsRed^{Tg}$ with PEdKO-$LysM^{GFP}$ parabionts using automatic tracking of cells with Imaris.

Intravital imaging of ischemia/reperfusion injury

Mouse cremaster were prepared as indicated without TNF-α stimulation. Upon exteriorization of the muscle we intravenously injected fluorescent antibodies to label cellular populations. Ly6G-APC (clone 1A8; BioXcell) for neutrophils, CD41-PE (eBioscience) for platelets, Ly6C-FITC (Biolegend) and CD62L-APC (BD Bioscience). Ischemia was achieved by occlusion of the incoming and outgoing vessels by clamping the tissue connecting the muscle and the animal's body with a 15mm Micro Serrefine clamp (Fine Science Tools, Heidelberg, Germany) for 45 minutes. Reperfusion was achieved by removal of the clamp. In some experiments neutrophils were depleted prior ischemia by injecting an anti-Ly6G-antibody (see below). Recordings were made with 3 second interval for 2 minutes for each field of view. Imaging was performed before and during ischemia, and during reperfusion. Some mice were treated intravenously with 300µg of Cl-amidine (Cayman Chemical Company, Ann Arbor) 1h before imaging, or with 500µg DNAse I (Roche, Basel, Switzerland) immediately before imaging.

Analysis of neutrophil clearance in the steady-state

11 to 18 week-old $DsRed^{Tg}$ mice were analysed after 1 month in parabiosis with non-fluorescent $CXCR2^{\Delta N}$, $CXCR4^{\Delta N}$, $Bmal^{\Delta N}$ and PEdKO mice or wild-type controls. The blood of each WT mice was analysed and used to obtain the ratio of neutrophils derived from each partner. Mice were sacrificed with CO_2 and carefully perfused with 30 ml of PBS to remove all blood. Tissues (white adipose tissue or WAT, large intestine, liver, lung, skin and spleen) were extracted and kept in cold PBS (except liver, kept at room temperature in HBSS) and processed immediately. Skin, large intestine (colon), lung and WAT were digested in HBSS with liberase (1U/ml, Roche) and DNAse I (1 mU/ml, Sigma) for 30 min at 37°C. Bone marrow and spleen were mechanically dissociated to prepare single-cell suspensions by flushing and straining, respectively. Enrichment of leukocytes in liver was performed by centrifugation using a 36% Percoll (GE Healthcare, diluted in HBSS) gradient. Colons were pre-incubated with HBSS containing 5mM EDTA for 45 min at 37°C before digestion to remove epithelial cells. Blood counts were analysed in an automated hemocytometer (Abacus Junior, Diatron; Holliston, USA) and blood red blood cells (RBC) lysed in a hypotonic buffer. Single-cell suspensions from tissues were incubated with fluorescently-conjugated antibodies against CD45, CD11b and Ly6G (BioXcell) and analysed in a Sony SP6800 Spectral Analyzer. DsRed+ $Ly6G^{hi}$ cells and $DsRed^{NEG}$ $Ly6G^{HI}$ cells discriminated host-(DsRedTg) from partner-derived neutrophils. To normalize values between the different parabiotic pairs we corrected the ratios of host vs. partner-derived neutrophils in each tissue with the ratios present in blood of each parabiotic pair. Deviations from the original ratio in blood was used to estimate the efficiency of migration of partner-derived neutrophils in each organ. Finally, infiltration efficiencies were normalized to the values obtained for the $DsRed^{Tg}$:WT pairs, which was set as the control group.

Quantification of neutrophil numbers in tissues

In some experiments, we measured absolute numbers of neutrophils present in tissues (see Neutrophil clearance assays). Truecount beads (Truecount absolute counting tubes, BD) were prepared at a concentration of 10,000 beads per ml of PBS buffer. 300µl of the bead suspension were added to single cell suspensions stained for flow cytometry, and then neutrophil number values were calculated based on the number of beads per tube and corrected by the weight or volume of tissue analysed.

Chemokine quantification in plasma

CXCL12, CXCL1 and CXCL2 levels were measured in plasma samples taken every 4h from WT mice using commercially available ELISA reagents, following the manufacturer's protocol (R&D Systems; Minneapolis; MN).

RNA-sequencing

Blood neutrophils were FACS sorted using by Ly6G and DAPI labelling, with typical purities > 95%. cDNA amplification from neutrophil RNA (1275pg) and generation of index-tagged sequencing libraries were carried out using the Ovation® Single Cell RNA-Seq System (NuGEN® Technologies, San Carlos CA). Libraries were quantified using a Quant-iTTM dsDNA HS assay with the Q-bit fluorometer (Life Technologies, Carlsbad, California). Average library size and size distribution were determined using a High Sensitivity DNA assay in an Agilent 2100 Bioanalyzer (Agilent Technologies, Santa Clara CA). Libraries were normalized to 10nM using Tris-Cl 10mM, pH8.5 with 0.1% Tween 20. Libraries were applied to an Illumina flow cell for cluster generation (True Seq SR Cluster Kit V2 cBot) and 61 nt long, single-end reads were generated on a Genome Analyzer IIx, using the TruSeq SBS Kit v5 (Illumina) and following the standard RNA sequencing protocol. Reads were further processed using the CASAVA package (Illumina) to demultiplex reads according to adapter indexes and to produce fastq files. Read quality was determined with the application FastQC (Schageman et al., 2013). The RNA sequencing experiments were performed at the Genomics Unit at CNIC.

Western Blotting

Blood neutrophils were sorted based on Ly6G (clone 1A8) expression. Purified cells were lysed in RIPA buffer containing 50 mM Tris-HCl, pH 8; 150 mM NaCl; 1% Triton X-100; 0.5% sodium deoxycholate; 0.1% SDS; 1mM PMSF (Sigma) and a protease inhibitor cocktail (Sigma). Proteins from $2x10^5$ lysed cells were separated by 10% SDS-PAGE and transferred onto PVDF membrane. Membranes were incubated overnight with antibodies against Bmal1 (Bethyl labs) and β-Actin (Abcam) at 1:1000 dilutions, and then thoroughly washed and incubated with HRP-conjugated anti-rabbit or anti-mouse antibody (1:1000; GE Healthcare Life Sciences). Blots were visualized using the chemiluminescent Luminata Forte Western HRP Substrate (Millipore).

Generation of transplant chimeras

To address the aging status of mutants in the same physiological context as wild-type cells, we generated mixed bone marrow chimeras, which has the added advantage of allowing simultaneous staining and analysis of willd-type and mutant cells. Donor BM cells were harvested

from DsRed^{Tg} or experimental models by flushing the femur with PBS. Recipient wild-type C57BL/6 mice were lethally irradiated (two 6Gy doses, 3 h apart) before receiving 1 million bone marrow nucleated cells by intravenous injection. For mixed chimeras, equal numbers of experimental and DsRed^{Tg} BM cells were mixed before intravenous injection. Engraftment of recipient animals was assessed 8–10 weeks after transplantation by analysis of the percentage of mutant and DsRed^{Tg} leukocytes in blood by flow cytometry.

Circadian analysis of aging markers and RNA extraction

Circadian blood samples were extracted every 4 h during 24 h from wild-type or experimental mice, starting at ZT1 (Zeitgeber time, 1 hour after the onset of light, 7:00 at the CNIC's animal facility). For circadian surface marker analysis, RBC were lysed in hypotonic lysis buffer (0.15M KH_4Cl, 0.01M KHCO3 and 0.01M EDTA in water) and incubated 15 minutes with 0.25 µg anti-Ly6G (1A8 clone, BioXcell), -CXCR2 (Biolegend) and -CXCR4 (eBioscience) antibodies, washed and analysed in a Sony SP6800 Spectral Analyser. Analysis was performed using Flowjo vX (Tree Star Inc, Ashland, OR). For circadian RNA assays, blood taken at above circadian time points was lysed for RBCs and sorted using a Sony SH800S Cell Sorter (Sony Biotechnology, Japan) based on viable Ly6G^{+} cells. RNA was extracted as indicated above.

Analysis of neutrophil aging in light-dark and dark-dark light regimes.

To check the circadian nature of neutrophil aging we compared twice a day (ZT5 and ZT13) the number of CD62L^{LO} aged neutrophils for 4 consecutive days in WT mice subjected to 12h:12h light: dark cycles, and in mice subjected to constant darkness in a light cabinet (LFC 3-16 with EF700ET programmer from E. Becker & Co) starting 24h after the onset of the light schedule. We analysed blood neutrophils at the indicated time points by flow cytometry as indicated above.

Entrainment of neutrophil aging by inverted light regime.

We maintained wild-type mice in 12h: 12h light-dark or dark-light (inverted light cycle) regimes using light-cabinets (Light/ Dark Chamber LT400 from Parkbio). After 3 weeks of this inverted regime we analysed peripheral blood neutrophils every 6 hours for 24 hours by flow cytometry, as indicated above.

Infection with *Candida albicans*

Mice were intravenously infected with 1.5x10^5 *C. albicans* conidia (SC5314 strain) and monitored daily for weight loss and general health following our institutional guidance. Infections were performed either at ZT5 or ZT13. Kidney fungal burden was determined at day 6 post-infection by plating organ homogenates in serial dilutions on YPD plates (Sigma); colony-forming units (CFUs) were counted after growth for 48 hr at 30ºC. Flow cytometry analysis of renal leukocyte infiltrates was performed on cell suspensions obtained from kidney homogenates obtained by digestion with 0.025 mg/ml of Liberase TL (Roche) for 10 min at 37ºC and filtered through 40 µm cell strainers (BD PharMingen). Phenotypic analyses of renal leukocyte infiltration were performed by flow cytometry.

Heat-killed *Candida albicans* (HKC) phagocytosis assay

Candida albicans conidia were heat-killed by boiling for 30 minutes. To quantify the phagocytic capacity, BM-sorted neutrophils were stained with 5 μM CFSE and exposed to labelled HKC labelled with 2.5 μM Cell Violet-labelled (both from Molecular probes) at a 30:1 ratio, for 15 min at 37º. After washing, cells were recovered on ice with PBS containing 5 mM EDTA. To remove bound but not internalized HKC, cells were incubated in Trypsin-EDTA (0.25%; Life Technologies) for 15 minutes at 37º prior to analysis by flow cytometry. Cells were fixed in 4% paraformaldehyde and neutrophils engulfing HKC were identified as double-positive cells for Cell Violet and CFSE. Cytospin preparations were also done for microscopic inspection of phagocytosis.

Mouse model of acute myocardial infarction

Male 8 to 12 week-old mice were subjected to 45 min occlusion of the left anterior descending (LAD) coronary artery followed by 1h reperfusion (for infarct size). For survival experiments, the LAD was reperfused for up to 24h and mice monitored hourly for the first 6h, and at 16, 20 and 24h. The I/R procedure was performed as previously described (Garcia-Prieto et al., 2017). In some experiments mice were depleted of neutrophils as indicated below. Briefly, fully anesthetized animals were intubated and temperature controlled throughout the experiment at 36.5°C to prevent hypothermic cardioprotection. Thoracotomy was then performed and the LAD was ligated with a nylon 8/0 monofilament suture for 45 min. The electrocardiogram was monitored (MP36R, Biopac Systems Inc.) to confirm total coronary artery occlusion (ST-segment elevation) throughout the 45 min ischemia. At the end of the ischemia, the chest was closed and animals were kept with 100% O_2 and analgesized with buprenorphine (subcutaneous injection, 0.1 mg/kg). For quantification of infarct size, mice were re-anesthetized and re-intubated, and the LAD coronary artery was re-occluded by ligating the suture in the same position as the original infarction. Animals were then sacrificed and 1 mL of 1% Evans Blue dye (Sigma) was infused IV to delineate the Area at Risk (AAR: myocardium lacking blood flow, i.e. negative for blue dye staining). The left ventricle (LV) was isolated, cut into transverse slices (5-7 1-mm thick slices per LV), and both sides were imaged. To delineate the infarcted (necrotic) myocardium, slices were incubated in triphenyltetrazolium chloride (TTC, Sigma) at 37 °C for 15 min. The slices were then re-photographed, weighed, and regions negative for Evans Blue staining (AAR) and for TTC (infarcted myocardium) were quantified using ImageJ (NIH, Bethesda, MD). Percentage values for AAR and infarcted myocardium were corrected to mg independently for each slice. Absolute AAR and infarct size were determined as the mg:mg ratio of AAR:LV and infarcted myocardium:AAR, respectively. Outcome assessment was performed blind to condition (mouse type, zeitgeber time or treatment).

Brain ischemia

To induce brain ischemia (without reperfusion injury) we followed previously described protocols (Sreeramkumar et al., 2014). Mice were anesthetized with isoflurane 1.5-2% in a mixture of 80% air / 20% oxygen, and body temperature was maintained at physiological levels with a heating pad during the surgical procedure and anaesthesia recovery. Mice were subjected to permanent focal cerebral ischemia (middle cerebral artery occlusion - pMCAO) through the distal occlusion of middle cerebral artery by ligature of the trunk just before its bifurcation between the frontal and parietal branches with a 9-0 suture, in combination with the occlusion of the ipsilateral common carotid artery. Following surgery, individual animals were returned to their cages with free access

to water and food. All the groups were performed and quantified in a randomized fashion by investigators blinded to groups. Physiological parameters were not significantly different among the different groups studied. Infarct size was determined by magnetic resonance imaging 48 hours after MCAO using a BIOSPEC BMT 47/40 (Bruker, Ettlingen, Germany). Infarct volume was calculated using the ImageJ software (NIH, USA) from the T2-weighted images. With the observer masked to the experimental conditions, the areas of the infarcted tissue (InfArea), the whole ipsilesional hemisphere (IpsArea) and the whole contralesional hemisphere (ContrArea) were delineated for each slice. Then, infarct volume, expressed as percentage of the hemisphere that is infarcted (%IH) was calculated using the formula: %IH = InfVol/ContrVol*100 where InfVol (Infarcted Tissue Volume) = $\Sigma InfArea_i$ / $SwellingIndex_i$, ContrVol (Contralesional Hemisphere Volume) = $\Sigma ContrArea_i$ and $SwellingIndex_i$ = $IpsArea_i/ContrArea_i$. Neutrophil quantification in brains was performed 48h after surgery. The ipsilateral cortex was dissected, placed in ice-cold PBS and dissociated into a single cell suspension by mechanical dissociation. Cell suspensions were filtered on 70-µm nylon mesh strainers and centrifuged at 300g for 10 min at room temperature. Pellets were resuspended in 8 mL of 35% Percoll and overlaid on the top of 5 ml HBSS. The gradient was centrifuged at 800*g* for 40 minutes at 4ºC and cell pellets resuspended for staining with anti-CD11b-FITC and anti-Ly-6G-PE antibodies (BD Bioscence). Stained cells were analysed in a FACSCalibur flow cytometer with CellQuest software (BD Pharmingen, San Jose, CA) and data was analysed using FlowJo software (Tree Star Inc, Ashland, OR).

Scanning electron microscopy

Blood from WT, $Bmal1^{\Delta N}$ and $CXCR4^{\Delta N}$ was harvested, RBC lysed and leukocytes stained with Ly6G (1A8, BioXcell) before sorting in a FACS Aria sorter (BD Biosciences). Sorted cells were immediately centrifuged and fixed using 4% PFA plus 2.5% glutaraldehyde in PBS for 2h at 4ºC. Cells were then dehydrated by serial 5 min incubations in increasing concentrations of ethanol, (30%>50%>70%>80%>90%>100%). Samples were dried in an automated critical point dryer (Leica EM CDP 300) and then coated in a rotary-pumped coating system (Quorum Technologies Q150RS). Imaging was performed at 10kV with a field emission microscope (JEOL 6335F). Critical point drying, coating and imaging of the samples was performed at ICTS National Centre of Electron Microscopy (UCM, Madrid, Spain).

CXCR2 and CXCR4 cross-inhibition assays

Wild-type mice were bled, RBC lysed and leukocytes resuspended in RPMI 1640 (Invitrogen). Some cells were pretreated with CXCL12 (50 ng/ml, R&D Systems) for 5 minutes at 37ºC while others were left untreated. Cells were allowed to migrate towards CXCL1 (50ng/ml, R&D Systems) or CXCL2 (50ng/ml, R&D Systems) through 6.5mm transwells with 5µm pore polycarbonate membrane insert (Corning, NY, USA), for 1h at 37ºC. Transmigrated cells were collected and stained with anti-Ly6G and anti-CD62L antibodies for cytometric analysis. Migration to only media was also used as a control. Quantification was performed using Truecount beads, as indicated above.

Neutrophil depletion

In some experiments mice were depleted of neutrophils prior to ischemia/reperfusion. Mice were injected 100µg of anti-Ly6G antibody (1A8 clone; BioXCell; West Lebanon, NH) intraperitoneally

for 2 consecutive days resulting in >93% reduction in blood neutrophil counts. Lymphocyte and monocyte counts were not affected by this treatment (Casanova-Acebes et al., 2013).

Zymosan-induced peritonitis

Transplantation chimeras or the wild-type partner in parabiotic pairs were treated with zymosan (1mg, intraperitoneal injection, Sigma). After 2 h we took blood samples and obtained the peritoneal lavage for cytometric analyses and cell count. We compared the ratios of neutrophils from each donor in the peritoneum and blood to estimate the migration efficiencies of mutant cells (ratio in peritoneum / ratio in blood). We also compared the migration efficiency of neutrophils in wild-type mice at ZT5 and ZT13. In this case we measured the absolute number of neutrophils in the peritoneal lavage using counting beads (Truecount absolute counting tubes, BD) and normalized migration relative to the absolute number of neutrophils in blood.

For experiments analyzing the dynamics of neutrophil aging during inflammation, we treated wild-type mice with zymosan (1mg, i.p.) and after 24h we analyzed blood neutrophils twice per day (ZT5 and ZT13) for 4 consecutive days. We estimated the absolute number of aged ($CD62L^{LO}$) neutrophils by flow cytometry as indicated above.

Soluble selectin binding assays

Transplantation chimeras were bled and RBC lysed, then cells washed in RPMI 1640 containing 5% FBS and stained them using E- or P-selectin/human IgM chimeras as reported (Hidalgo et al., 2007). Cells were further incubated for 15 min with a FITC-conjugated anti-human IgM (Jackson Immunoresearch) and anti-Ly6G-APC (BioXcell) antibodies. Control samples contained 5mM EDTA. Cells were analysed in a Sony SP6800 Spectral Analyzer.

Auto-perfused flow chamber assay

In order to investigate the number of rolling and adherent cells, we used a microflow chamber system (Zarbock et al., 2007). 20 x 200 ⌈m rectangular glass capillaries were filled with P-selectin (50 ⌈g/ml) alone or in combination with ICAM-1 (15 µg/ml) and/or CXCL1 (25 ⌈g/ml) for 2 hr and blocked for 2 hr with 1% casein (Pierce Chemicals, Dallas, TX). One side of the chamber was connected to a PE 10 tubing and inserted into the carotid artery. The other side of the chamber was connected to a PE 50 tubing and used to control the wall shear stress, which was calculated as described (Zarbock et al., 2007). Microscopy was conducted with a Zeiss Axioskop (Carl Zeiss, Inc., Thornwood, NY) with a saline immersion objective (SW 20, N.A. 0.5). Recordings were taken using an SW40/0.75 objective and a digital camera (Sensicam QE). Capturing on P-selectin was analyzed after 2 minutes and chemokine-induced arrest was analyzed after 6 minutes of perfusion.

Cortical beta-actin quantification

Sorted neutrophils were cytospun onto Superfrost Plus microscope slides (Thermo Scientific, Waltham, USA) with a Shandon Cytospin 4 (Thermo Scientific) for 5 minutes at 500 RPM in medium acceleration. Then cells were fixed with 4% PFA in PBS for 10 minutes and blocked with 5% goat serum, 5% BSA in saline in a humid chamber for 30 minutes. Finally, cells were stained with a rabbit anti-mouse beta-actin antibody (ab8227, Abcam) and with a secondary goat anti-rabbit antibody conjugated with AF568. Then slides were mounted with Mowiol and captured with

a Leica SP8 X confocal microscopy system. Analysis of captured images was performed using Imaris (Bitplane).

ROS quantification

Red blood cell-lysed blood was plated in RPMI in 96-well polystyrene microplates (Corning Falcon, New York, USA) and stimulated with 50nM of phorbol 12-myristate 13-acetate (PMA) for 1h. Cells were then stained with 5mM Dihydroethidium (DHE, Thermo Fisher, Waltham, USA) for 20 minutes and stained for cytometric analysis.

Chemotaxis assay

Whole blood was harvested and red blood cells were lysed. Cells were plated in 6.5mm polycarbonate transwells with 5µm pores (Corning, Corning, USA) in RPMI medium. In the bottom well, a single chemokine was added to allow chemotactic migration: 25mg/ml CXCL12 (R&D), 20ng/ml CXCL1 (R&D), 5ng/ml LTB4 (Tocris), 100mM fMLP (Sigma) or 10ng/ml CCL2 (R&D). Transwells were incubated 2h at 37ºC and transmigrated cells were harvested from the bottom well and stained for cytometric analysis. The number of transmigrated cells was assessed by the presence of a known number of Truecount beads (BD Biosciences).

Multiplex cytokine assay.

Mice were i.p. injected with Zymosan as indicated above. After 2 hours peritoneal lavages were collected and neutrophils stained for FACS sorting. One million sorted neutrophils were incubated for 3h in RPMI containing 0.5% BSA and 100,000 heat-killed *C. albicans* conidia. Supernatants were collected and frozen at -80ºC until cytokine quantification was performed. CXCL1, IL-10, IL-1β, IL-12, TNFα, G-CSF, IL-23, CXCL2, IL-6 and CCL2 were measured in neutrophil supernatants using the Mouse ProcartaPlex™ Multiplex Immunoassay (PPX-10-MXTZ766), following the manufacturer's protocol (Thermo Scientific, Waltham, USA). For TGF-β1 detection, samples were activated with HCl and measured using commercial TGF beta-1 Mouse ProcartaPlex™ Simplex Kit (EPX01A-20608-901). Data acquisition was performed on a MagPix instrument (Luminex Inc, Houston, TX) using xPONENT v4.2 software (Luminex) and analyzed with ProcartaPlex Analyst software (v1.0; Thermo Scientific).

AMD3100-induced neutrophilia

2.5mg/kg of AMD3100 (Tocris) was injected intraperitoneally into wild-type mice 1h before analysis. Then blood neutrophils were analyzed at ZT5 in an automated hemocytometer (Abacus Junior) and stained for cytometric analysis as previously described. At this time (1h after injection of AMD3100) we subjected control or AMD3100-treated mice to AMI and *Candida albicans* infection, as previously described.

Neutrophil transfer experiments.

To increase the yield of fresh neutrophils we used AMD3100-treated mice as neutrophil donors (see Figure S5G). To minimize ex vivo manipulation of neutrophils we transferred 200 µl of freshly extracted blood from donor mice by i.v. injection into host wild-type mice at ZT5. Aging markers in host and donor cells were then analyzed 5 minutes and 5 hours after inoculation in the peripheral blood of host mice by flow cytometry as indicated above.

BrdU labelling

For metabolic labelling with 5-Bromodeoxyuridine, mice were intraperitoneally injected with a single dose of 2.5mg BrdU (BD Biosciences). Blood samples were collected at indicated times and stained for Ly6G, CD62L, CXCR2 and CXCR4, followed by fixation and intracellular labelling of BrdU using an APC-conjugated anti-BrdU antibody as per manufacturer's instructions (BD Biosciences).

In vivo CXCL1 and CXCL2 blockade

For in vivo blockade of CXCL1 and CXCL2, mice were injected intraperitoneally twice with 50μg of isotype or monoclonal antibody against CXCL1 (MAB453, R&D) or CXCL2 (MAB452, R&D) the night before the analysis (-17h) and the same day (-5h). Blood from treated mice was harvested and analysed by flow cytometry as previously described. In a set of mice, intravital imaging was performed to analyse neutrophil behaviour in the microvasculature of the cremaster muscle by intravital microscopy as previously described.

Cecal ligation and puncture (CLP)-induced sepsis

CLP was performed as previously described (Rittirsch et al., 2009). Briefly, the peritoneal cavity of ketamine/xylazine-anesthetised mice was exposed with a small incision and the cecum was exteriorized. 80% of the cecum distal to the ileo-cecal valve was ligated using non-absorbable 7-0 suture. A 23-gauge needle was then used to puncture both walls of the distal end of the cecum, and a small drop of faeces was extruded through the perforation. The ligated and punctured cecum was relocated inside the peritoneal cavity and both peritoneum and skin were closed. Mice were then treated with s.c. injection of Buprenorphine. Control mice (sham) were included with the same procedure but without ligation or puncture.

Evans blue vascular permeability assay.

To address whether the constitutive presence of fresh or aged neutrophils in the mutant mice affected the vascular integrity, we performed vascular permeability assays as previously described (Radu and Chernoff, 2013). Briefly, a 0.5% solution of Evans blue in sterile PBS was prepared and 200μl of the solution was i.v. injected into WT or mutant mice. 5 minutes after the transfer mice were sacrificed and tissues extracted and weighted. Then, tissues were submerged in 1ml formamide and incubated at 50ºC for 24h. Tissues were removed and the tubes centrifuged for 5 minutes at 645 g. Finally, supernatants were measured for absorbance at 610nm using an xMark Microplate Spectrophotometer (BioRad) plate reader. The vascular permeability test was performed in untreated and LPS-treated (10 mg/kg) mice.

Analysis of endothelial proliferation and apoptosis.

We processed tissues from WT or mutant mice as previously described (see section Analysis of neutrophil clearance in the steady-state) to obtain single cell suspensions. One half of the suspension was used to measure apoptosis and the rest to assess proliferation. For proliferation we measured Ki67 by intra-nuclear staining in endothelial cells. Cells were stained with anti-CD45 conjugated with PerCP/Cy5.5 (BioLegend) and anti-CD31-APC (eBioScience) and then fixed and permeabilized using the Fix/Perm and Perm Buffers (eBiosciences) according to manufacturer's

instructions. Cells were then stained for 20 minutes at 4ºC with an anti-mouse/rat Ki67 antibody labelled with eFluor660 (Thermo Fisher) and analysed by flow cytometry.
For quantification of apoptotic endothelial cells we measured Annexin V binding and DAPI labelling. Cell suspensions were incubated with 1:200 of anti-CD45 and anti-CD31, washed twice in cold PBS and resuspended in Annexin V Binding Buffer (10 mM Hepes, pH adjusted to 7.4 with NaOH, 140 mM NaCl, 2.5 mM $CaCl_2$) at a concentration of 1 million cells per ml. 100µl of this cell suspension ($1x10^5$ cells) was stained with PE-conjugated Annexin V (Invitrogen) for 15 minutes at room temperature in the dark. Finally, 400µl of binding buffer containing DAPI was added to each tube and analyzed by flow cytometry within one hour.

Analysis of neutrophil aging in microbiota depleted and germ-free mice.
For microbiota depletion studies we followed a previously published protocol (Zhang et al., 2015). Briefly, mice were fed with a cocktail of antibiotics (ABX) including ampicillin (1 g/l), neomycin (1 g/l), metronidazol (1 g/l) and vancomycin (1 g/l) in drinking water for 4 weeks prior to analysis by flow cytometry. For germ-free mice we compared by flow cytometry SPF-housed with germ free (GF) mice for markers of aging state (see method of Circadian analysis of aging markers and RNA extraction).

QUANTIFICATION AND STATISTICAL ANALYSIS

Specific quantification protocols are detailed in each method above.

RNA-sequencing data analysis
For data analysis, sequencing adaptor contaminations were removed from reads using Cutadapt and the resulting reads were mapped on the transcriptome (GRCm38 Ensembl gene-build 70) and quantified using RSEM v1.17 (Li and Dewey, 2011). Only genes with at least one count per million in at least 2 samples were considered for statistical analysis. Data were then normalized and differential expression tested using the Bioconductor package EdgeR (Robinson et al., 2010). Raw and Benjamini-Hochberg adjusted p-values were calculated for each of the comparisons of interest. Non-adjusted p-values were used to identify overrepresented pathways using Ingenuity Pathway Analysis (IPA, Quiagen, www.ingenuity.com). These results were quantitatively validated by qPCR analyses for a collection of relevant genes, and functionally validated using *in vivo* assays as detailed in the manuscript. K-means clustering, PCA analysis and heat-map representations were produced using the Genesis software (Sturn et al., 2002).

Statistical analysis
Unless otherwise indicated, data are represented as mean values ± standard error of the mean (SEM). Paired or unpaired t-test was used when 2 groups were compared, and comparison of more than two data sets was done using one-way analysis of variance (ANOVA) with Turkey's post-test. Where applicable, normality was estimated using D'Agostino & Pearson or Shapiro-Wilk normality test. Log-rank analysis was used for Kaplan-Meier survival curves. Sample

exclusion was not performed unless evident signs of disease were found in a mouse, in which case statistically significant outliers were identified using Grubb's test (ESD method). Comparisons of two time curves were performed using two-way ANOVA. All statistical analyses were performed using Prism v6 (GraphPad Software, California, USA). A p-value below 0.05 was considered statistically significant; non-significant differences (ns) are indicated accordingly.

Amplitude vs zero test

For determination of diurnal patterns, we performed COSINOR fitting of circadian curves, using the curve-fitting module of Graphpad Prism with the equation Y = Baseline + Amplitude x cos (Frecuency X + Phaseshift), where Baseline = average of Ymax and Ymin; Amplitude = 0.5 x (Ymax – Ymin), Frecuency=0.2618 ($2*\pi/24$) and Phaseshift= value of X at Ymax. To determine whether a diurnal curve displayed an oscillating pattern we used the COSINOR-calculated amplitudes and compared them with a hypothetical zero-amplitude curve (i.e. with no circadian behaviour) assuming that both curves have identical standard deviations. We finally compared the two curves' amplitudes using unpaired t-test analyses. This analysis gave a better estimation of circadian patterns considering all time points rather than comparing only two times. Through the text this is termed "amplitude vs zero test".

DATA AND SOFTWARE AVAILABILITY

Raw data for the RNA sequencing analyses can be publicly accessed at the Gene Expression Omnibus (GEO, NCBI) with GEO Accession Number GSE102310 (for reviewers: https://www.ncbi.nlm.nih.gov/geo/query/acc.cgi?acc=GSE102310; password for reviewers: knkzmwsenvannir). Any other pieces of data are available on request.

KEY RESOURCES TABLE

REAGENT or RESOURCE	SOURCE	IDENTIFIER
Antibodies		
CXCR4-APC (Human)	eBioscience	Clone 12G5; RRID:AB_1944349
CD11b-FITC (Human)	eBioscience	Clone ICRF44
CD16-Pacific Blue (Human)	BD	Clone 3G8
CD62L-PE (Human)	BD	Clone DREG56
CD11c-APC (Human)	BD	Clone B-ly6
bio	eBioscience	Clone 1A8
Ly6G-Dylight 450	BioXcell (conjugated in-house)	Clone 1A8; RRID:AB_1107721
Ly6G-Dylight 650	BioXcell (conjugated in-house)	Clone 1A8; RRID:AB_1107721
Ly6G-FITC	eBioscience	Clone 1A8; RRID:AB_2572532
CD45-PerCP-Cy5.5	Biolegend	Clone 30-F11; RRID:AB_893344
CD11b-PE	Tonbo Biosciences	Clone M1/70; RRID:AB_2621746
CD11b-FITC	BD	Clone M1/70; RRID:AB_394774
CXCR2-PerCP-Cy5.5	Biolegend	Clone SA044G4; RRID:AB_2565695
CXCR4-APC	eBioscience	Clone 2B11; RRID:AB_10670877
CD41-PE	eBioscience	Clone MWReg30 RRID:AB_2538354
Ly6C-FITC	Biolegend	Clone HK1.4
CD62L-APC	eBioscience	Clone MEL-14; RRID:AB_469410
CD62L-FITC	eBioscience	Clone MEL-14; RRID:AB_465109
Anti-CXCL1	R&D	MAB453; RRID:AB_2087696
Anti-CXCL2	R&D	MAB452; RRID:AB_2230058
Anti-CXCL12	R&D	MAB350; RRID:AB_2088149
Anti-Ly6G (depleting antibody)	BioXCell	BE0075-1; RRID:AB_1107721
Experimental Models: Organisms/Strains		
WT	Charles River	C57BL/6
$Mrp8^{CRE}$	Passegué et al. 2004	B6.Cg-Tg(S100A8-cre,-EGFP)1Ilw
$CXCR2^{fl/fl}$	Schloss et al. 2016	$C57BL/6\text{-}Cxcr2^{tm1Rmra}$
$CXCR2^{\Delta N}$	This paper	N/A
$CXCR4^{fl/fl}$	Nie et al. 2004	$B6.129P2\text{-}Cxcr4^{tm2Yzo}$
$CXCR4^{\Delta N}$	This paper	N/A
$CXCR4^{WHIM}$	Balabanian et al. 2012	$Cxcr4^{/1013}$
$Arntl^{fl/fl}$	Janich et al. 2011	$B6.129S4(Cg)\text{-}Arntl^{tm1Weit}$
$Bmal1^{\Delta N}$	This paper	N/A
PEdKO	Frenette et al. 1996	$B6.129S2\text{-}Sele^{tm1Hyn}\ Selp^{tm1Hyn}$
DsRED	Vintersten et al. 2004	B6.Cg-Tg(CAG-DsRed*MST)1Nagy
LysM-GFP	Faust et al. 2000	$B6.129P\text{-}Lyz2^{tm1(EGFP)1.1Graf/Mmmh}$
Chemicals, Peptides, and Recombinant Proteins		
CXCL12 (recombinant)	R&D	460-SD

CXCL1 (recombinant)	R&D	453-KC
CXCL2 (recombinant)	R&D	452-M2
TNFα	R&D	410-MT-050
AMD3100	Tocris	Cat#3299
Oligonucleotides		
Primers for qPCR, see table S3	This paper	N/A
Software and Algorithms		
ImageJ	NIH	Schindelin J. et al 2015
Imaris	Bitplane	RRID:SCR_007370
Genesis	TÜ Graz	RRID:SCR_015775
Prism	Graphpad	RRID:SCR_002798
Flowjo vX	Treestar	RRID:SCR_008520

Supplemental Information

A neutrophil timer coordinates immune defense and vascular protection

José M. Adrover, Carlos del Fresno, Georgiana Crainiciuc, Maria Isabel Cuartero, María Casanova-Acebes, Linnea A. Weiss, Héctor Huerga Encabo, Carlos Silvestre-Roig, Jan Rossaint, Itziar Cossío, Ana V. Lechuga-Vieco, Jaime García-Prieto, Mónica Gómez-Parrizas, Juan A. Quintana, Ivan Ballesteros, Sandra Martin-Salamanca, Shu Zhen Chong, Maximilien Evrard, Karl Balabanian, Jorge López, Kiril Bidzhekov, Françoise Bachelerie, Francisco Abad-Santos, Cecilia Muñoz, Alexander Zarbock, Oliver Soehnlein, Christian Weber, Lai Guan Ng, Cristina López-Rodriguez, David Sancho, María A. Moro, Borja Ibáñez and Andrés Hidalgo

Supplemental figures

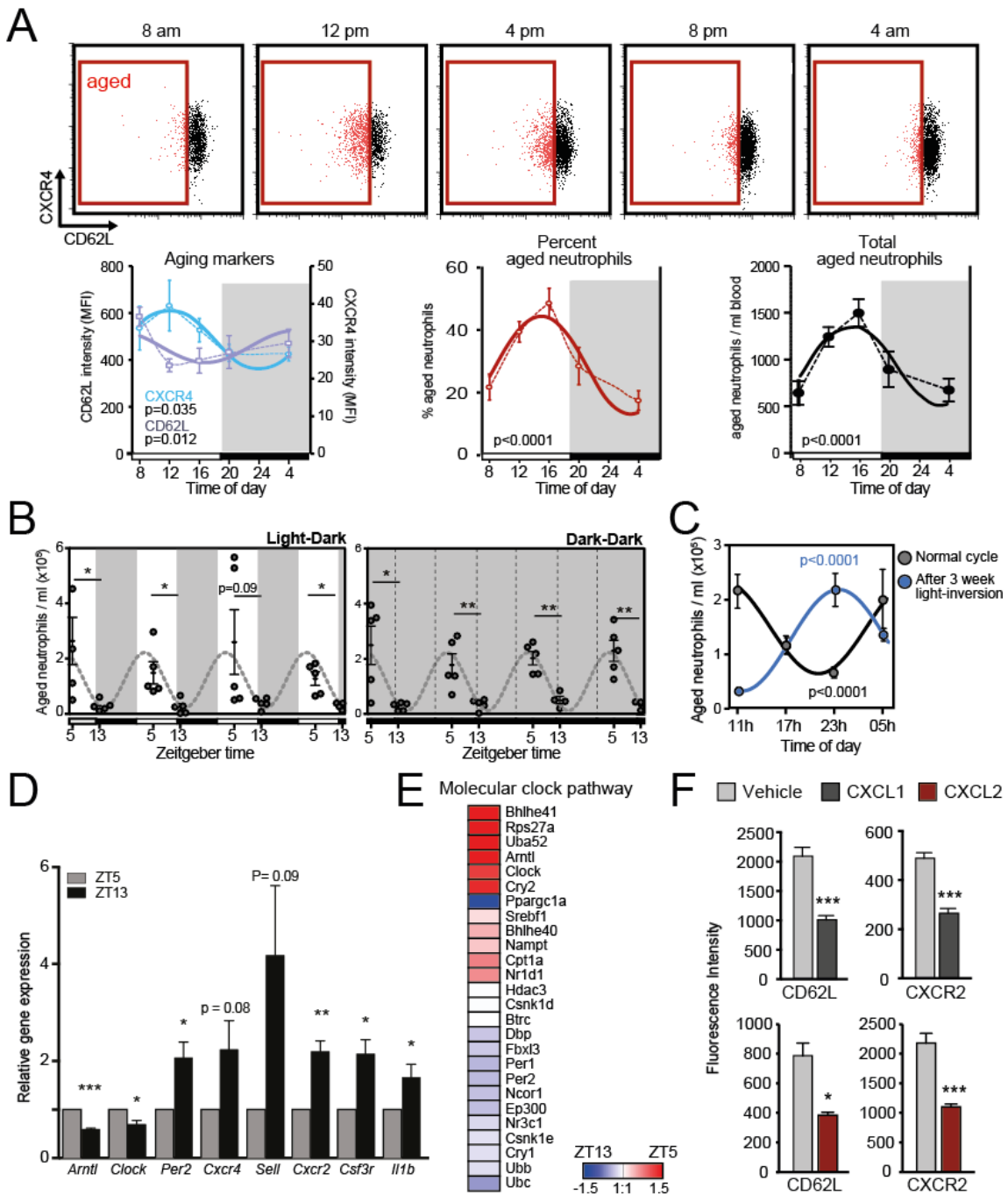

Figure S1. Patterns of neutrophil aging in humans and mice, related to **Figure 1.**
(A) Evidence of aging in human neutrophils. Blood samples from healthy volunteers (n=6 for markers; 12 for percent and total aged) were taken at the indicated times, analyzed with a hemocounter and by flow cytometry. Top panels, representative cytometry plots of human blood samples, gated on DAPI^{NEG}, CD11b+, CD16+ neutrophils and further stained for CXCR4 and CD62L. Lower panels show the levels of CD62L and CXCR4 on neutrophils at different diurnal times (left panel) which were used to calculate the percentage (middle panel) and total number

(right panel) of aged neutrophils. The indicated P values were calculated after Cosinor adjustment as indicated in the Methods section (amplitude vs. zero test).
(B) Diurnal patterns of aging are preserved in constant darkness. The phenotype and number of neutrophils was estimated for 4 consecutive days at ZT5 and ZT13 by flow cytometry (CD62L staining), in mice maintained under LD (left) or DD (right). Data from n=3-5 mice per time.
(C) Entrainment of diurnal aging by light. Mice were kept in a 12h light-shift schedule for 3 weeks before analyzing the number of aged neutrophils throughout a full diurnal cycle in control or light-shifted mice. Data from n=5 mice per time. P values were calculated as in (A).
(D) Validation of diurnally regulated genes in mouse neutrophils. Quantitative PCR of selected genes identified from the RNAseq analyses as differentially regulated between ZT5 and ZT13 (n=3-7). Values are mean ± SEM. *, p<0.0.5; **; p<0.01; ***, p<0.001 as determined by unpaired t-test analysis.
(E) Fold-change expression of genes of the molecular clock pathway as determined from the RNAseq analyses of circulating neutrophils purified at ZT5 and ZT13.
(F) Ex vivo treatment with the CXCR2 agonists CXCL1 or CXCL2 induces downregulation of CD62L and CXCR2 on neutrophils; n=4-10. These changes resemble those seen during diurnal aging, as shown in Figure 1E.
Data are presented as mean ± SEM. *, p<0.05; **, p<0.01; ***, p<0.001 as determined by unpaired t-test analysis, except as indicated (A and C).

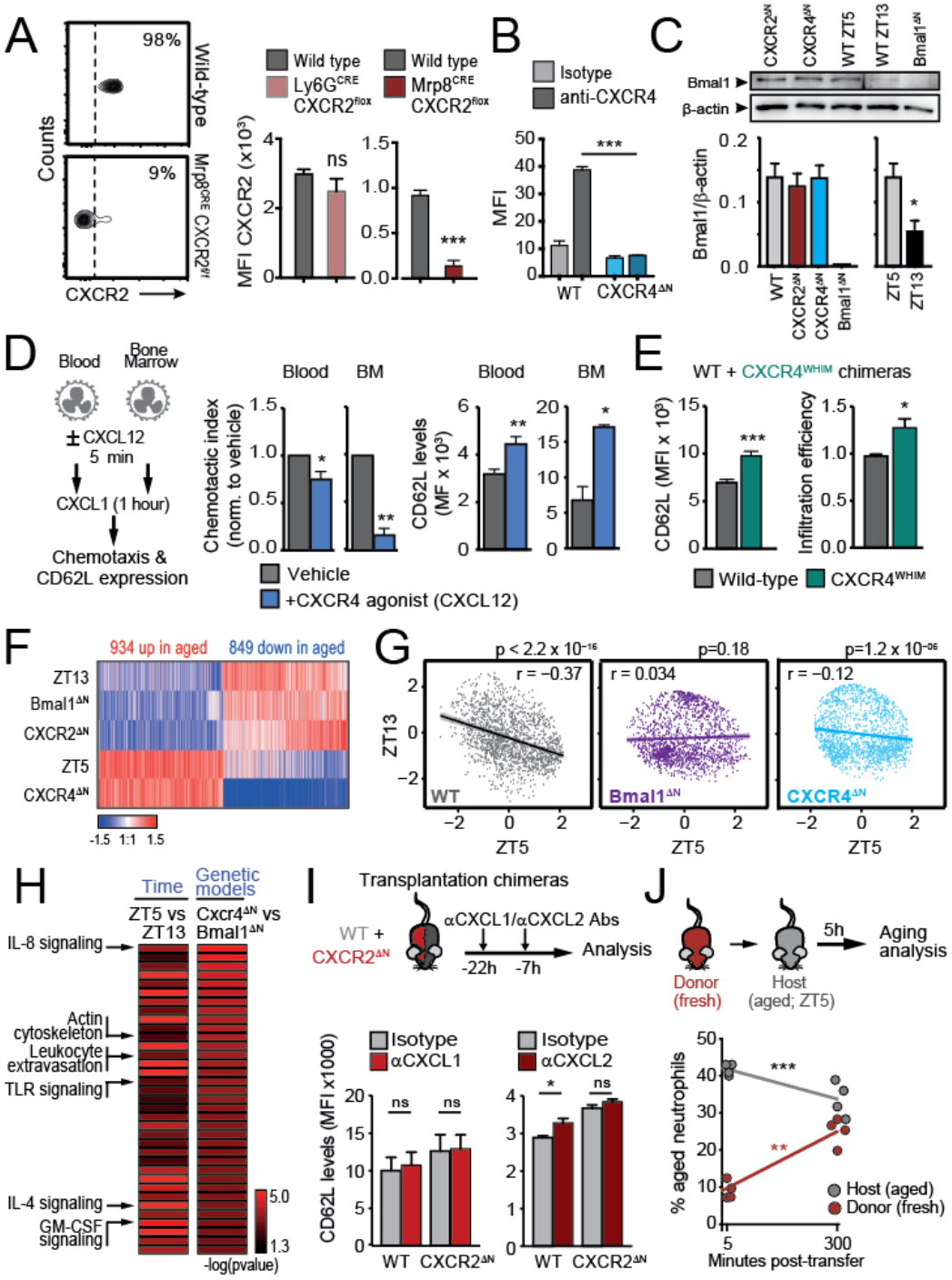

Figure S2. Validation of differentially expressed genes and diurnal regulation of genes of the molecular clock pathway, related to **Figure 2.**

(A) Depletion of CXCR2, CXCR4 and Bmal1 from neutrophils. To establish specific and robust gene-deletion in neutrophils in vivo we tested two different existing drivers. The highly-specific Ly6G^{CRE} driver (Hasenberg et al., 2015) is poorly efficient for CXCR2$^{FL/FL}$ excision, as assessed by flow cytometry. Instead, the MRP8^{CRE} driver (Passegue et al., 2004) allows efficient deletion in CXCR2^{floxed} mice, as shown in the density plots (left); n=4-12 mice per group.

(B) Efficient and specific deletion of CXCR4 in $CXCR4^{fl/fl}$ mice using the $MRP8^{CRE}$ driver, as determined by flow cytometry of blood neutrophils with isotype or anti-CXCR4 antibodies; n=3.
(C) Bmal1 protein levels in wild-type and mutant blood neutrophils. For wild-type neutrophils we measured protein levels at ZT5 and ZT13. Blots are shown on top, and quantification corrected for β-actin load control are shown in the bar graphs at bottom; n=3 independent experiments.
(D) Inhibition of CXCR2 signaling through CXCL12/CXCR4. Wild-type neutrophils were pre-incubated with CXCL12, a CXCR4 agonist, and then allowed to migrate towards a CXCL1 gradient. The number of migrated cells and their expression of CD62L was evaluated by flow cytometry n=2 (bone marrow) and 5 (blood).
(E) Analysis of CD62L levels in neutrophils from transplant chimeras of wild-type and $CXCR4^{WHIM}$ donors; n = 5 mice.
(F) Heat map showing the transcriptomic fingerprint of fresh and aged groups, showing coherent changes between fresh (ZT13, $Bmal1^{\Delta N}$ and $CXCR2^{\Delta N}$) and aged neutrophils (ZT5 and $CXCR4^{\Delta N}$).
(G) Scatter plots showing signature genes (from Figure S2F) of neutrophils from wild-type, $Bmal1^{\Delta N}$ or $CXCR4^{\Delta N}$ mice, comparing their profiles at ZT5 vs. ZT13. Note that diurnal variation in the profile is most prominent for wild-type cells and blunted for $CXCR4^{\Delta N}$ and $Bmal1^{\Delta N}$ cells.
(H) Functional pathways differentially regulated both in circulating neutrophils over time (ZT13 vs ZT5) and between genetic models ($Bmal1^{\Delta N}$ vs. $CXCR4^{\Delta N}$). We used a criterion of –log (p-value)>1.3 to select these pathways using the IPA package, the most relevant of which are indicated.
(I) Experimental set-up to test the effect of in vivo blocking CXCL1 or CXCL2 on CD62L levels in circulating neutrophils from WT:$CXCR2^{\Delta N}$ transplantation chimeras; n=3-7. CXCL2 partially blocks loss of CD62L in wild-type cells, but has no effect in $CXCR2^{\Delta N}$ neutrophils.
(J) Neutrophil aging after transfer. Experimental set-up and percentage of aged ($CD62L^{LO}$) neutrophils at 5 min and 5h after transfer. Fresh donor cells age over time while host aged neutrophil are reduced; n=4 donor and 4 recipient mice.
Data are presented as mean ± SEM. *, $p<0.05$; ***, $p<0.001$; n.s., not significant, as determined by unpaired (A-E) or paired (I-J) t-test analysis; ns, not significant.

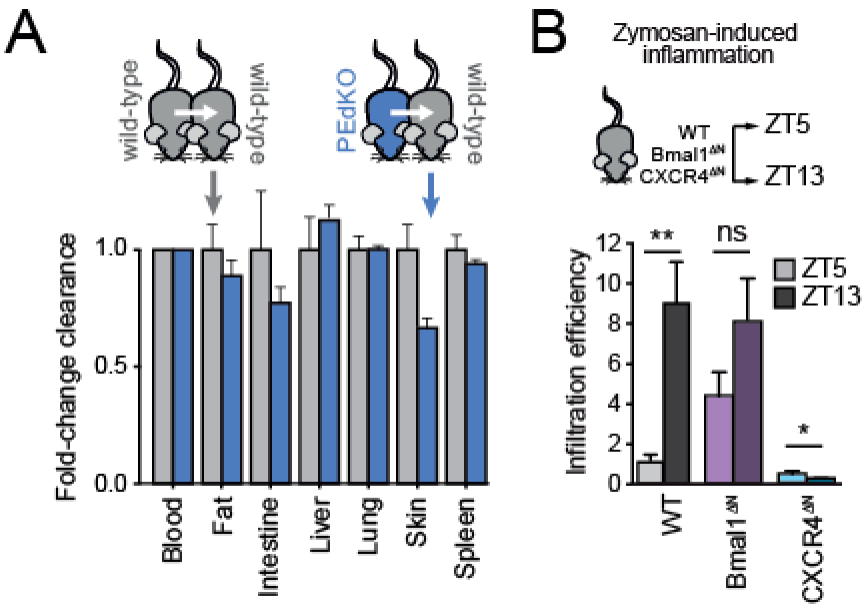

Figure S3. Migratory properties of fresh and aged neutrophils, related to **Figure 3.**
(A) Homeostatic clearance of WT or aged (PEdKO) neutrophils into the tissues of wild-type parabiotic partners. WT:WT parabionts were used as reference; n=3-8.
(B) Migration efficiency of neutrophils into the peritoneum of zymosan-treated wild-type, Bmal1$^{\Delta N}$ and CXCR4$^{\Delta N}$ mice at ZT5 or ZT13. The infiltration efficiency was corrected by the number of neutrophils present in the circulation at those times; n=5-7 per group and time.
Data are presented as mean ± SEM. *, $p<0.05$; **, $p<0.01$ as determined by unpaired t-test analyses.

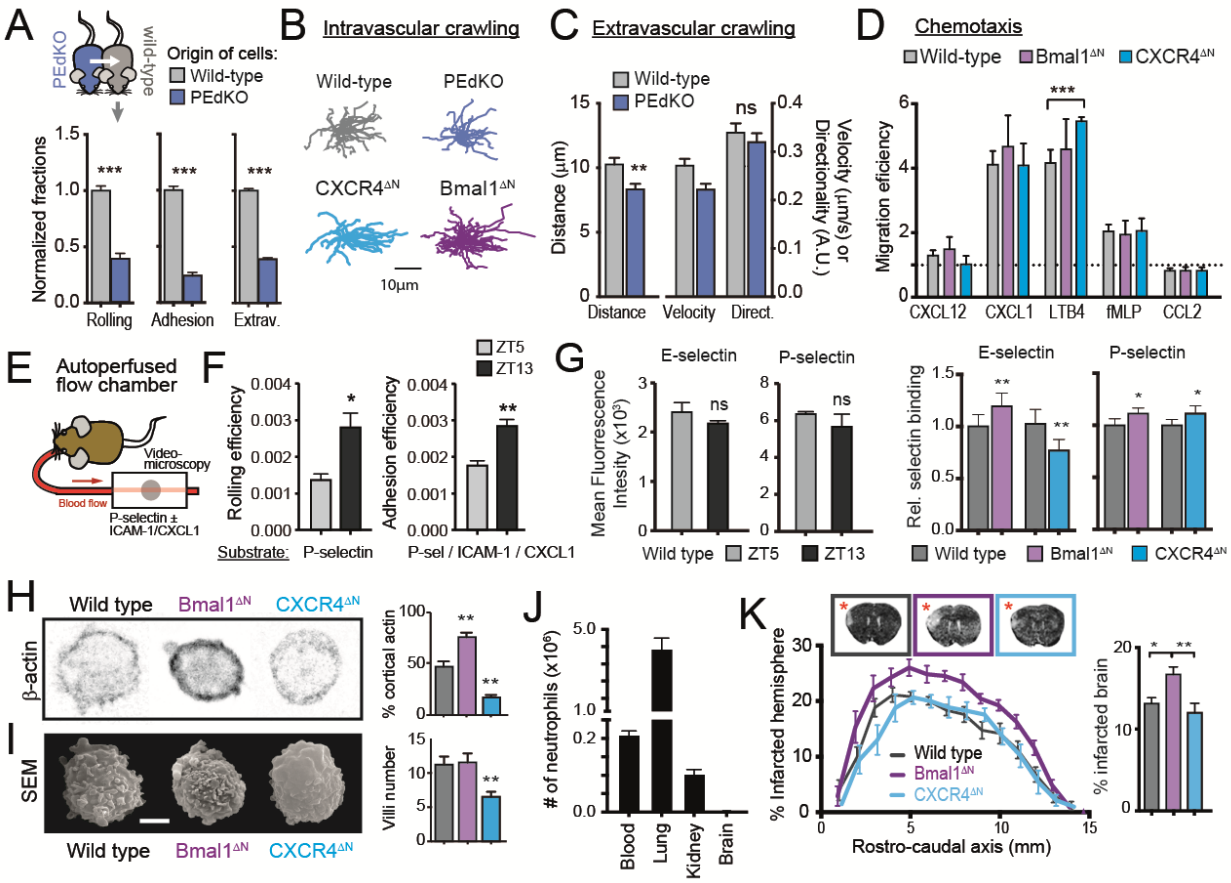

Figure S4. Differential rolling and migration of neutrophils at different diurnal times and from aging mutants, related to **Figure 4.**

(A) Parabiosis of PEdKO with wild-type partners to evaluate the migration of aged (PEdKO) vs wild-type neutrophils into inflamed tissues of the wild-type partner. Bars show the fractions of neutrophils from each partner that rolled, adhered and extravasated in the microcirculation of the inflamed cremaster muscle (TNFα-treated); n=28-53 venules for rolling/adhesion, and 10,021 cells for extravasation, from 3-5 parabiotic pairs.

(B) Crawling tracks of neutrophils of wild-type, fresh (Bmal1$^{\Delta N}$) and aged (CXCR4$^{\Delta N}$ and PEdKO^{GFP}) neutrophils within inflamed cremasteric vessels, as assessed by intravital microscopy. PEdKO neutrophils were analyzed in the parabiosis setup shown in (A), whereas Bmal1$^{\Delta N}$ and CXCR4$^{\Delta N}$ neutrophils were analyzed from the BM chimeras shown in Figure 3A-B. No significant differences were found for velocity, distance or directionality. Data is from 30-61 cells from 3-6 mice.

(C) Dynamics of wild-type and aged (PEdKO^{GFP}) neutrophils extravasated into the interstitial tissue of inflamed cremaster muscles. Data was obtained from the same animals shown in (A); Data is from 30-33 cells from 3 parabiotic pairs.

(D) Chemotactic efficiencies of wild-type and mutant cells towards common neutrophil chemokines and chemoattractants. The dashed line indicates migration to media alone; n=4-11 replicates.

(E-F) Diurnal variations in rolling efficiency are neutrophil-intrinsic. (E) Experimental scheme of the autoperfused flow chamber. Endogenous wild-type neutrophils roll in a flow chamber coated with P-selectin alone, or together with ICAM-1 and CXCL1 to induce adhesion. (F) Rolling and

Adhesion efficiencies of neutrophils from mice analyzed in the flow chambers at ZT5 or ZT13; n=4 mice per time.

(G) Selectin ligands in fresh and aged neutrophils. Quantification of selectin binding by neutrophils from wild-type mice at ZT5 and ZT13 (left), or from wild-type and mutant mice at ZT5 (right); n=4-5 mice per group.

(H) Immunofluorescence staining of β-actin in wild-type, Bmal1$^{\Delta N}$ and CXCR4$^{\Delta N}$ neutrophils, and frequency of neutrophils with cortical distribution of β-actin (ZT5); n=122-301 cells per group.

(I) Scanning electron micrographs of wild-type, Bmal1$^{\Delta N}$ and CXCR4$^{\Delta N}$ neutrophils, and quantification of the number of villi on their surface (ZT5). Scale bar, 2 μm; n=26-29 cells per group.

(J) Number of neutrophils at baseline in different tissues of wild-type mice. Note the absence of neutrophils in the brain. Values are per ml blood or gram of tissue; n=4 mice.

(K) Percentage of infarcted brain areas along the rostro-caudal axis, and representative images, from wild-type, Bmal1$^{\Delta N}$ and CXCR4$^{\Delta N}$ mice. Infarcts were performed at ZT5. Asterisks identify infarcted areas; n=8-11 mice per group. Bar-graphs at right show the percentage of infarcted brain volumes in the groups shown in (K)

Data are presented as mean ± SEM. *, $p<0.05$; **, $p<0.01$; ***, $p<0.001$, ns, not significant, as determined by paired (A, C) or unpaired (D, F, G, H) t-test analysis, or one-way ANOVA with Dunnett's multiple comparison test (H, I, K).

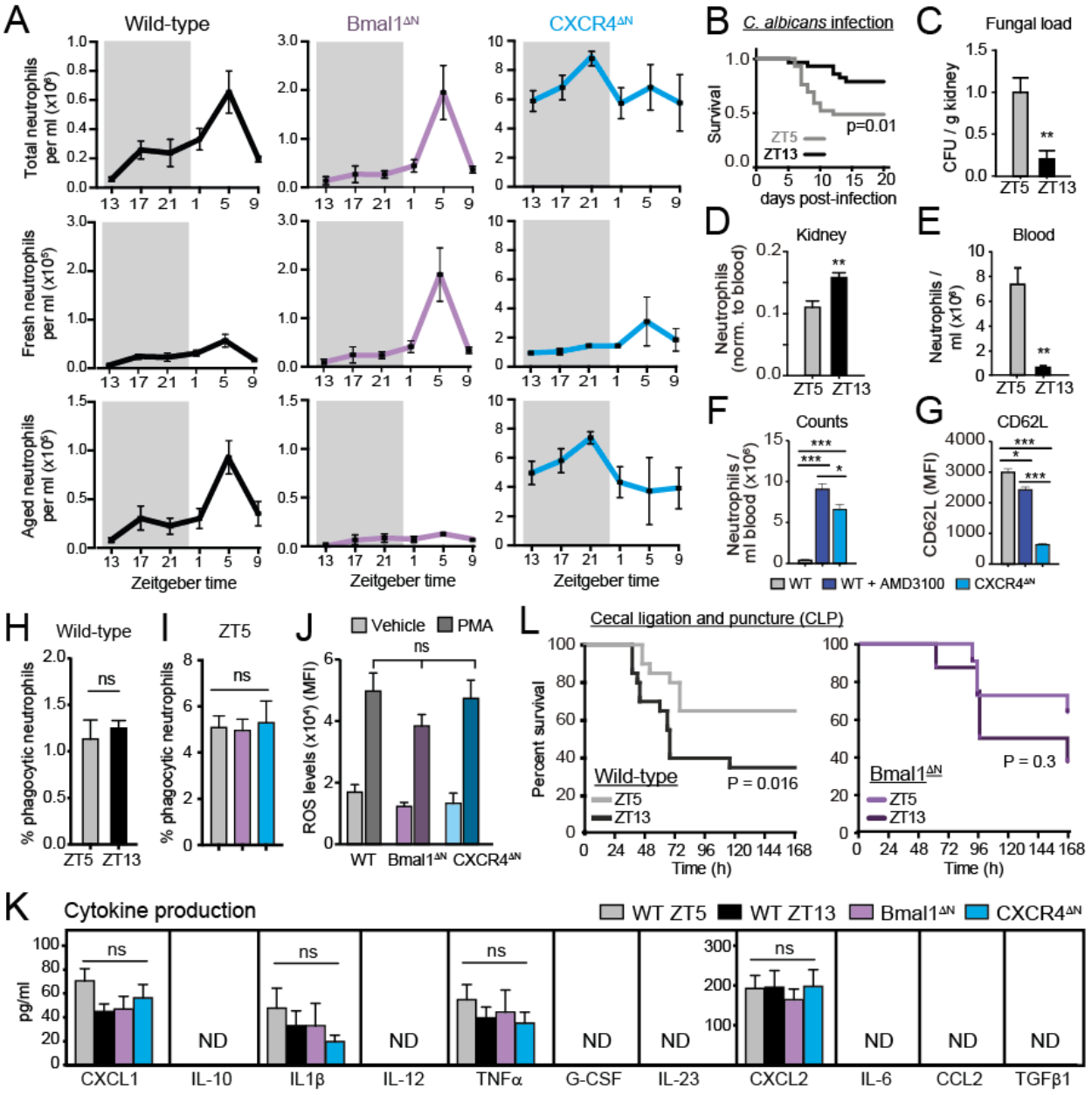

Figure S5. Diurnal patterns of circulating neutrophils and responses to infection, related to **Figure 5.**

(A) Diurnal dynamics of total, fresh and aged neutrophils in wild-type, Bmal1$^{\Delta N}$ and CXCR4$^{\Delta N}$ mice. Neutrophil numbers were obtained with a hemo-counter, and the frequency and absolute number of CD62L^{LO} aged and CD62L^{HI} fresh neutrophils estimated by flow cytometry; n = 32-56 mice per group. Note the different scales across the different groups. Shaded areas correspond to night time.

(B) Survival curves of wild-type mice infected with *C. albicans* at ZT5 or ZT13 and monitored for 20 days; n=27-29 mice. P value was calculated by the log rank (Mantel-Cox) test.

(C) Fungal load at sacrifice in the kidneys of mice shown in (B).

(D) Number of neutrophils in naïve kidneys at the indicated times, with values normalized to blood counts at each time; n= 5 mice per group.
(E) Diurnal variations in neutrophil numbers in the circulation of the same mice as (D) at ZT5 and ZT13; n=5 mice per time point.
(F) Neutrophil counts in wild-type mice, wild-type mice treated with AMD3100 and CXCR4$^{\Delta N}$ mice at ZT5; n=3-4 mice per group.
(G) Levels of surface CD62L on neutrophils from the mice shown in (F).
(H-I) Phagocytic efficiency measured as the percentage of phagocytic neutrophils that take up fluorescently-labeled heat-killed *C. albicans*, from wild-type mice at ZT5 and ZT13, or (H) from wild-type and mutant mice at ZT5; n=3-6.
(J) ROS production measured by DHE oxidation by flow as determined by flow cytometry in wild-type and the indicated mutant neutrophils treated with vehicle or PMA; n = 3 mice.
(K) Ex vivo cytokine production by neutrophils from the indicated sources and challenged with zymosan plus heat-killed *Candida*; n=4. ND, not detectable.
(L) Susceptibility to septic shock during cecal ligation and puncture (CLP). Survival curves of wild-type and Bmal1$^{\Delta N}$ mice subjected to CLP at ZT5 or ZT13, and followed for 7 days; n=8-20 mice per group. P values were calculated by the log rank (Mantel-Cox) test.
Except for (B and L), data are presented as mean ± SEM. *, $p<0.05$; **, $p<0.01$; ***, $p<0.001$, ns, not significant, as determined by unpaired (C, D, E and H) t-test analysis, or one-way ANOVA with Dunnett's multiple comparison test (F, G, I and J) or Tukey's multiple comparison test (K).

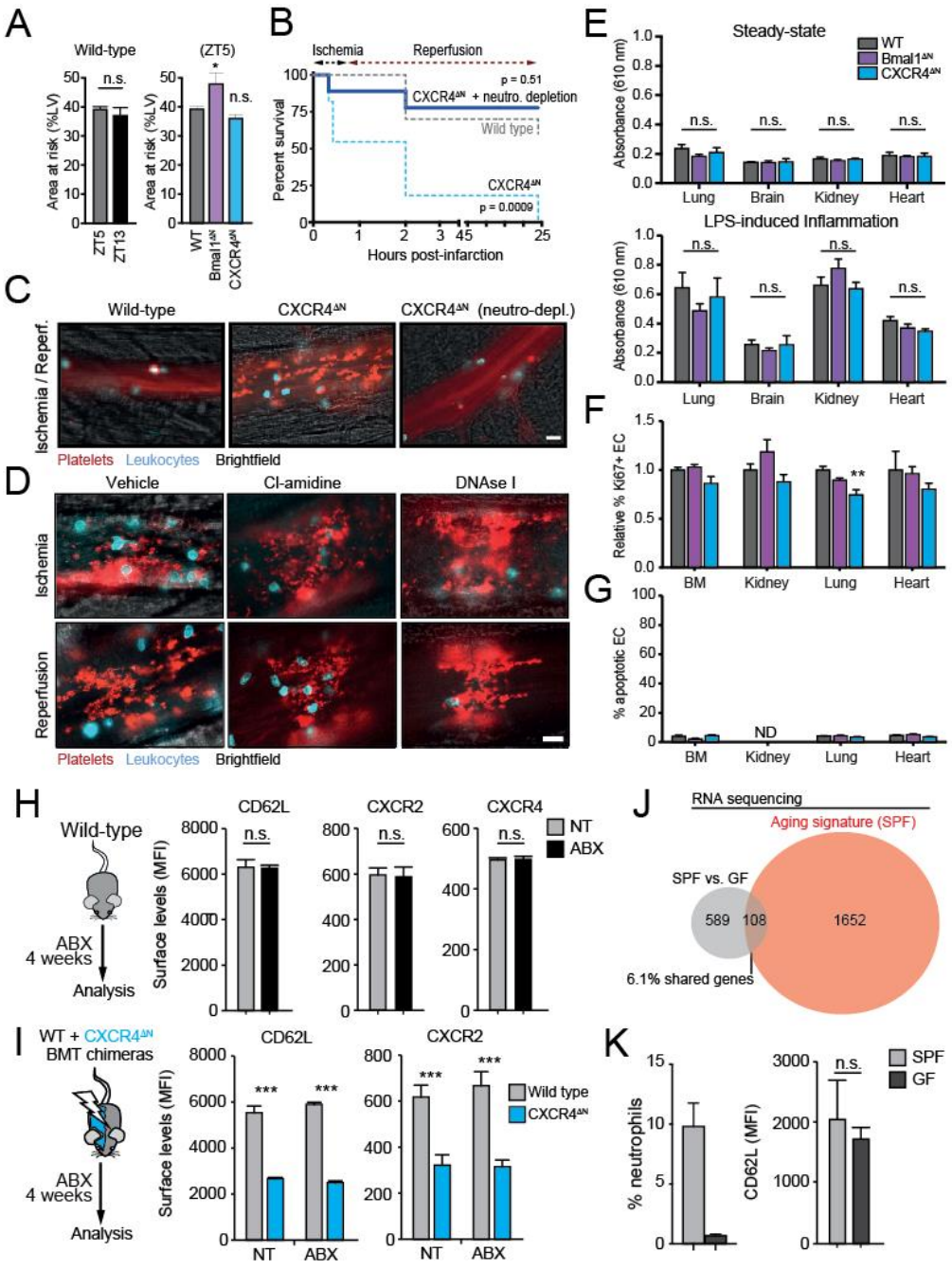

Figure S6. Myocardial infarction and intravascular thrombosis in wild-type and mutant mice, related to **Figure 6.**

(A) Areas at risk of the myocardium in the indicated wild-type and mutant mice subjected to ischemia of the coronary artery at ZT5 or ZT13 as indicated, followed by one hour of reperfusion. These values correspond to the groups shown in Figure 6B-C.

(B) Survival curves showing that neutrophil depletion rescues CXCR4$^{\Delta N}$ mice from AMI-induced death. Wild-type and CXCR4$^{\Delta N}$ mice, or CXCR4$^{\Delta N}$ mice depleted of neutrophils before being subjected to ischemia of the coronary artery for 45 min followed by 24 hour reperfusion. Data from 9-11 mice per group. P values compare against wild-type mice using the log-rank test.

(C) Intravital images of cremasteric venules re-perfused after 45 min of ischemia, showing accumulation of small thrombi within venules of CXCR4$^{\Delta N}$ mice, but not in wild-type mice or in CXCR4$^{\Delta N}$ mice after neutrophil depletion; images are representative of 3 mice. Bar, 10 μm.
(D) Representative images obtained by intravital microscopy of ischemic (top) and reperfused (bottom) cremasteric venules from CXCR4$^{\Delta N}$ mice treated with vehicle, or the NET inhibitors Cl-amidine or DNAse I. Note the persistence of micro-thrombi after treatment with either inhibitor, indicating that NETs are not responsible for platelet deposition in these mice; n = 3 mice.
(E) *V*ascular permeability in wild-type, Bmal1$^{\Delta N}$ and CXCR4$^{\Delta N}$ mice. Untreated mice (top) or LPS- treated mice were injected i.v. with Evans Blue and the presence of the dye in homogenized tissues analyzed by absorbance at 610nm; n= 5 per tissue and group.
(F) Percentage of proliferating CD31+ endothelial cells (EC) in the indicated tissues of wild-type, Bmal1$^{\Delta N}$ and CXCR4$^{\Delta N}$ mice and normalized to the wild-type group; n=4 mice per tissue and group.
(G) Percentage of apoptotic cells in the indicated tissues as measured by annexin V binding in EC; n=4 mice per tissue and group.
(H) Neutrophil phenotype measured by CD62L, CXCR2 and CXCR4 levels in control and antibiotics (ABX)-treated WT mice; n= 9-10 mice.
(I) Neutrophil phenotype in BM chimeras, showing no effect of microbiota depletion (ABX) in the aging phenotype of WT and CXCR4$^{\Delta N}$ neutrophils; n= 5 mice per group.
(J) Lack of transcriptional match between neutrophil aging and microbiota-induced gene expression, as shown by comparing the microbiota signature (SPF vs GF) with the aging signature (see Fig.S2F). RNAseq data from blood neutrophils from 2 SPF vs. 2 GF mice.
(K) GF mice display the expected neutropenia (left panel), but do not show phenotypic aging measured by CD62L levels (right panel); n=3 mice.
Data are shown as mean ± SEM; *, $p<0.05$; **, $p<0.01$; n.s., not significant, as determined by unpaired t-test (left panel in A, H, I and K), one-way ANOVA with Dunnett's multigroup correction (right panel in A, E, F and G), and Log-rank test (B).

Table S1. Complete list of canonical pathways differentially expressed in wild-type neutrophils at ZT5 (fresh) vs ZT13 (aged). Related to Figure 1.
Differentially-regulated pathways (-Log (p value)>1.3) were identified using the Ingenuity Pathway Analysis package. Ratios indicate the fraction of differentially expressed genes that map to the pathway, out of the total number of genes in that pathway.

Pathway	-Log(pvalue)	Ratio
EIF2 Signaling	16,60	0,23
B Cell Receptor Signaling	12,10	0,20
iCOS-iCOSL Signaling in T Helper Cells	10,20	0,23
PKCθ Signaling in T Lymphocytes	9,37	0,21
Role of NFAT in Regulation of the Immune Response	8,36	0,17
Regulation of eIF4 and p70S6K Signaling	8,08	0,18
B Cell Development	7,62	0,36
mTOR Signaling	7,51	0,16
PI3K Signaling in B Lymphocytes	7,31	0,18
Altered T Cell and B Cell Signaling in Rheumatoid Arthritis	6,68	0,21
IL-4 Signaling	6,27	0,21
Role of NFAT in Cardiac Hypertrophy	6,19	0,15
NF-κB Signaling	5,98	0,15
Chronic Myeloid Leukemia Signaling	5,63	0,18
HGF Signaling	5,50	0,17
T Cell Receptor Signaling	5,37	0,18
CD28 Signaling in T Helper Cells	5,35	0,16
Renin-Angiotensin Signaling	5,26	0,17
Calcium-induced T Lymphocyte Apoptosis	4,96	0,20
SAPK/JNK Signaling	4,92	0,17
EGF Signaling	4,87	0,21
Primary Immunodeficiency Signaling	4,81	0,23
Dendritic Cell Maturation	4,73	0,13
FcγRIIB Signaling in B Lymphocytes	4,68	0,24
IL-3 Signaling	4,45	0,18
T Helper Cell Differentiation	4,45	0,18
GM-CSF Signaling	4,40	0,19
Role of JAK1 and JAK3 in γc Cytokine Signaling	4,40	0,19
IL-2 Signaling	4,38	0,21
NF-κB Activation by Viruses	4,32	0,18
IL-6 Signaling	4,31	0,15
Type II Diabetes Mellitus Signaling	4,31	0,15
MSP-RON Signaling Pathway	4,21	0,22
CD40 Signaling	4,19	0,19
fMLP Signaling in Neutrophils	4,15	0,15
ErbB2-ErbB3 Signaling	4,07	0,19
Docosahexaenoic Acid (DHA) Signaling	4,06	0,23
Ephrin A Signaling	4,05	0,21
RANK Signaling in Osteoclasts	4,05	0,16
Telomerase Signaling	4,04	0,15
Colorectal Cancer Metastasis Signaling	4,01	0,11
Cardiac Hypertrophy Signaling	4,00	0,11

Acute Myeloid Leukemia Signaling	3,95	0,17
Reelin Signaling in Neurons	3,95	0,17
PEDF Signaling	3,81	0,17
Melanoma Signaling	3,80	0,21
CXCR4 Signaling	3,79	0,13
Endometrial Cancer Signaling	3,74	0,19
IL-9 Signaling	3,73	0,24
Gα12/13 Signaling	3,73	0,14
GNRH Signaling	3,73	0,13
Production of Nitric Oxide and Reactive Oxygen Species in Macrophages	3,70	0,12
NGF Signaling	3,66	0,14
p70S6K Signaling	3,65	0,13
Lymphotoxin β Receptor Signaling	3,60	0,19
Molecular Mechanisms of Cancer	3,59	0,09
Phospholipase C Signaling	3,58	0,11
phagosome formation	3,57	0,14
Non-Small Cell Lung Cancer Signaling	3,54	0,17
Role of Macrophages, Fibroblasts and Endothelial Cells in Rheumatoid Arthritis	3,51	0,10
Angiopoietin Signaling	3,48	0,17
Nitric Oxide Signaling in the Cardiovascular System	3,45	0,14
Nur77 Signaling in T Lymphocytes	3,40	0,18
Macropinocytosis Signaling	3,37	0,16
RAR Activation	3,37	0,11
Thrombin Signaling	3,37	0,11
Myc Mediated Apoptosis Signaling	3,34	0,17
Role of p14/p19ARF in Tumor Suppression	3,30	0,23
Rac Signaling	3,27	0,14
Fcγ Receptor-mediated Phagocytosis in Macrophages and Monocytes	3,23	0,14
Gap Junction Signaling	3,23	0,12
Prostate Cancer Signaling	3,21	0,15
Renal Cell Carcinoma Signaling	3,20	0,16
P2Y Purigenic Receptor Signaling Pathway	3,15	0,13
IL-8 Signaling	3,15	0,11
Insulin Receptor Signaling	3,14	0,12
Melanocyte Development and Pigmentation Signaling	3,11	0,14
LPS-stimulated MAPK Signaling	3,10	0,15
CNTF Signaling	3,07	0,17
IGF-1 Signaling	3,06	0,13
Gαq Signaling	3,06	0,12
FLT3 Signaling in Hematopoietic Progenitor Cells	3,05	0,15
Leptin Signaling in Obesity	3,05	0,15
Glioma Signaling	3,02	0,13
Role of Tissue Factor in Cancer	3,02	0,13
HER-2 Signaling in Breast Cancer	2,95	0,15
Breast Cancer Regulation by Stathmin1	2,95	0,11
PDGF Signaling	2,90	0,14

Thrombopoietin Signaling	2,89	0,16
Virus Entry via Endocytic Pathways	2,89	0,14
Erythropoietin Signaling	2,83	0,15
Hereditary Breast Cancer Signaling	2,79	0,12
GDNF Family Ligand-Receptor Interactions	2,78	0,15
Ceramide Signaling	2,76	0,14
Autoimmune Thyroid Disease Signaling	2,74	0,17
CREB Signaling in Neurons	2,74	0,11
Antigen Presentation Pathway	2,73	0,19
PTEN Signaling	2,73	0,12
Clathrin-mediated Endocytosis Signaling	2,73	0,10
PPAR Signaling	2,72	0,13
Xenobiotic Metabolism Signaling	2,72	0,09
Graft-versus-Host Disease Signaling	2,68	0,17
Glioblastoma Multiforme Signaling	2,67	0,11
IL-12 Signaling and Production in Macrophages	2,66	0,11
Glucocorticoid Receptor Signaling	2,65	0,09
Fc Epsilon RI Signaling	2,63	0,12
ErbB4 Signaling	2,62	0,15
LXR/RXR Activation	2,62	0,12
JAK/Stat Signaling	2,59	0,14
Role of Osteoblasts, Osteoclasts and Chondrocytes in Rheumatoid Arthritis	2,59	0,10
Signaling by Rho Family GTPases	2,58	0,09
Natural Killer Cell Signaling	2,56	0,12
FGF Signaling	2,55	0,13
TR/RXR Activation	2,55	0,13
AMPK Signaling	2,54	0,10
PPARα/RXRα Activation	2,54	0,10
p53 Signaling	2,53	0,12
Role of Pattern Recognition Receptors in Recognition of Bacteria and Viruses	2,49	0,11
NRF2-mediated Oxidative Stress Response	2,49	0,10
Estrogen-Dependent Breast Cancer Signaling	2,47	0,14
IL-15 Signaling	2,47	0,14
Role of PI3K/AKT Signaling in the Pathogenesis of Influenza	2,47	0,14
UVA-Induced MAPK Signaling	2,43	0,13
DNA Double-Strand Break Repair by Non-Homologous End Joining	2,42	0,29
Cell Cycle: G1/S Checkpoint Regulation	2,42	0,14
IL-17A Signaling in Airway Cells	2,42	0,14
VEGF Family Ligand-Receptor Interactions	2,42	0,13
G-Protein Coupled Receptor Signaling	2,42	0,09
Acute Phase Response Signaling	2,41	0,10
UVB-Induced MAPK Signaling	2,40	0,15
Leukocyte Extravasation Signaling	2,40	0,10
Systemic Lupus Erythematosus Signaling	2,37	0,09
Tec Kinase Signaling	2,36	0,10
Huntington's Disease Signaling	2,36	0,09
CCR3 Signaling in Eosinophils	2,32	0,11

Regulation of IL-2 Expression in Activated and Anergic T Lymphocytes	2,30	0,13
Neurotrophin/TRK Signaling	2,29	0,13
Germ Cell-Sertoli Cell Junction Signaling	2,28	0,10
IL-10 Signaling	2,24	0,13
HMGB1 Signaling	2,23	0,11
Glioma Invasiveness Signaling	2,20	0,14
Growth Hormone Signaling	2,20	0,13
GPCR-Mediated Integration of Enteroendocrine Signaling Exemplified by an L Cell	2,12	0,13
Small Cell Lung Cancer Signaling	2,12	0,13
Aldosterone Signaling in Epithelial Cells	2,12	0,10
Superpathway of Geranylgeranyldiphosphate Biosynthesis I (via Mevalonate)	2,09	0,24
Prolactin Signaling	2,04	0,12
ErbB Signaling	2,04	0,12
Toll-like Receptor Signaling	2,01	0,12
Neuropathic Pain Signaling In Dorsal Horn Neurons	2,01	0,11
eNOS Signaling	2,01	0,10
Mitochondrial Dysfunction	2,01	0,09
Endothelin-1 Signaling	1,98	0,09
ERK/MAPK Signaling	1,98	0,09
TREM1 Signaling	1,97	0,12
Antiproliferative Role of Somatostatin Receptor 2	1,94	0,13
Communication between Innate and Adaptive Immune Cells	1,94	0,11
PAK Signaling	1,94	0,11
CD27 Signaling in Lymphocytes	1,89	0,14
Acetate Conversion to Acetyl-CoA	1,87	0,50
IL-1 Signaling	1,87	0,11
Death Receptor Signaling	1,84	0,11
VEGF Signaling	1,84	0,11
Pancreatic Adenocarcinoma Signaling	1,84	0,10
Relaxin Signaling	1,82	0,10
Role of IL-17A in Arthritis	1,81	0,13
Mouse Embryonic Stem Cell Pluripotency	1,75	0,11
Oxidative Phosphorylation	1,75	0,10
Sphingosine-1-phosphate Signaling	1,75	0,10
Actin Cytoskeleton Signaling	1,71	0,08
Mevalonate Pathway I	1,64	0,23
Cholecystokinin/Gastrin-mediated Signaling	1,59	0,10
FAK Signaling	1,58	0,10
α-Adrenergic Signaling	1,58	0,10
Ethanol Degradation II	1,57	0,14
Colanic Acid Building Blocks Biosynthesis	1,55	0,21
Selenocysteine Biosynthesis II (Archaea and Eukaryotes)	1,50	0,33
Thioredoxin Pathway	1,50	0,33
ERK5 Signaling	1,47	0,11
April Mediated Signaling	1,44	0,13
VDR/RXR Activation	1,44	0,10

Regulation of the Epithelial-Mesenchymal Transition Pathway	1,43	0,08
Salvage Pathways of Pyrimidine Ribonucleotides	1,42	0,10
PI3K/AKT Signaling	1,41	0,09
Granzyme B Signaling	1,39	0,19
Atherosclerosis Signaling	1,39	0,09
PXR/RXR Activation	1,38	0,11
3-phosphoinositide Biosynthesis	1,37	0,08
B Cell Activating Factor Signaling	1,35	0,13
Superpathway of Cholesterol Biosynthesis	1,34	0,14
Corticotropin Releasing Hormone Signaling	1,34	0,09
Role of NANOG in Mammalian Embryonic Stem Cell Pluripotency	1,34	0,09
Unfolded protein response	1,32	0,11
2-amino-3-carboxymuconate Semialdehyde Degradation to Glutaryl-CoA	1,31	1,00

Legends to Supplementary Movies

Movie S1. Defective recruitment of aged neutrophils during inflammation. The video shows three sequences during the recruitment of neutrophils derived from wild-type^{GFP} (expressing LysM^{GFP}; green) and PEdKO^{RED} (expressing DsRed; red) partners, in the cremasteric microcirculation of the wild-type partner after TNFα treatment. In all steps of recruitment (rolling, adhesion and extravasation) wild-type^{GFP} neutrophils outperform aged neutrophils from the PEdKO^{RED} partner, even if the initial number of PEdKO-derived neutrophils was higher in the free circulation (not shown). In the second sequence (Adhesion), intravascular neutrophils are identified by labelling with anti-Ly6G (blue). Movies are representative of experiments from 3-5 mice, and are accelerated 3.6-fold for rolling and 24-fold for adhesion and extravasation. Quantification for these experiments is provided in Figure S4A.

Movie S2. Firm arrest of neutrophils to the microvasculature in the steady-state does not require rolling. Movies were acquired in the naïve dermal microcirculation at ZT9, and neutrophils were labelled with a fluorescent anti-Ly6G antibody. Movies at left show three examples from wild-type mice; movies at right show neutrophils from mice lacking endothelial selectins (PEdKO), in which rolling is impaired. In wild-type animals, rolling preceded but was dispensable for arrest, as demonstrated in the selectin-deficient mice. In the absence of selectins neutrophils undergo sudden arrest to the vasculature without engaging in rolling, as shown in Figure 4F. Dashed lines delineate the vessel wall. Scale bar, 10 μm. Movies are accelerated 24-fold.

Movie S3. Neutrophil-dependent formation of intravascular thrombi during ischemia-reperfusion in CXCR4$^{\Delta N}$ mice. Ischemia was induced by clamping feeding arteries of the cremaster muscle in wild-type or CXCR4$^{\Delta N}$ mice for 45 min before reperfusion. Movies were acquired during the ischemic and early reperfusion phases. Platelets are labelled with anti-CD41 antibodies and leukocytes with anti-Ly6G or anti-CD62L plus anti-Ly6C antibodies. Thrombi bound to the vessel wall appeared only in the CXCR4$^{\Delta N}$ mice, and disappeared when neutrophils were depleted (CXCR4$^{\Delta N}$ neutrophil-depleted). Scale bars, 10 μm. Movies are accelerated 24-fold. See also Figure S6C.

Movie S4. Neutrophil aging ensures diurnal defense and vascular protection. Diurnal aging of neutrophils released from the bone marrow (fresh neutrophils) is driven by Bmal1 through control of CXCL2 production and CXCR2 signaling, and is opposed by CXCR4. During aging neutrophils alter their surface topology and lose microvilli. As a result, aged neutrophils display impaired rolling and recruitment to inflamed tissues, but can naturally migrate to non-inflamed tissues (homeostatic clearance) through sudden arrest that does not require rolling. Aged neutrophils in tissues fight potential infections (*C. albicans* in kidneys) but can cause vascular damage if present in the circulation during ischemia-reperfusion (myocardial infarction). Fresh neutrophils that infiltrate inflamed tissues promote damage during sterile tissue inflammation (brain ischemia).